Universidad del País Vasco
Euskal Herriko Unibertsitatea

ZIENTZIA ETA TEKNOLOGIA FAKULTATEA
FACULTAD DE CIENCIA Y TECNOLOGÍA

Bachelor Final Project
Chemical Engineering

Effect of supporting MnO_X-CeO_2 for the simultaneous catalytic abatement of NO_X and PCDD/Fs at MSWI plants

Author
Cristina Camara Garcia

Directors
Asier Aranzabal Maiztegi
María Pilar González Marcos

Leioa, 18 June 2021

INDEX

1. INTRODUCTION

Waste management is an environmental, technical, and economical challenge. Currently, the human activity based on a consumerist economy and a culture of one time use products, generates tons of waste. The European Directive (2008/98/CE) establishes municipal solid waste (MSW) as the solid waste from households (mixed or separately collected) including paper, cardboard, glass, metals, plastics, bio-wastes, wood, textiles, containers, wastes of electric and electronic systems, batteries, and accumulators, as well as other bulkier ones, such as mattresses and furniture. Not only are municipal wastes the ones with domestic origin, but they also are the ones coming from other sources, when due to their nature and composition can be assimilated as the previous. Thus, it consists of everyday items we use and then throw away (Neuwahl et al., 2019).

According to the data of Eurostat, in the year 2018, the total waste generated by all economic activities and households amounted to 2317 million tonnes (5200 kilograms per inhabitant) in the European Union, from which the 8.2% (approximately 190 million tonnes, ca. 490 kilograms per capita) corresponded to household wastes. This amount of household wastes has risen a 5.9% from 2004 to 2018.

From these 190 million tonnes of total household waste, approximately 23 million correspond to those created in Spain (475 kg/capita, 17.7% of the total Spanish waste amount). The most developed countries in the European Union, the ones located in the north, e.g., Germany, Denmark, Luxemburg, Finland, and Norway, create more MSW per inhabitant compared to Spain. These countries are among the European countries with the highest gross domestic product per capita. Reversely, in poorer countries, such as Lithuania, Croatia, North Macedonia, and Hungary, the production of MSW per inhabitant is smaller.

To deal with this situation the necessity of regulations is undeniable. For this reason, the Directive 2008/98/CE of the European Parliament, which is the main regulatory instrument to combat this situation, has established the following hierarchy of waste: the first and most important one would be prevention; followed by preparation for reuse; recycling; other forms of recovery; ending up with removal. In The European Directive (2018/851) it can be found which are the current economic instruments and other measures to provide incentives for the application of the mentioned waste hierarchy. This is the case of "Pay-as-you-throw" schemes that charge waste producers on the basis of the actual amount of waste generated and provide incentives for separation at source of recyclable waste and for reduction of mixed waste. Other examples are the support to research and innovation in advanced recycling technologies and remanufacturing. As well as economic incentives for regional and local authorities, in particular to promote waste prevention and intensify separate collection schemes, while avoiding support to landfilling.

Significant differences in waste management schemes are found around the world depending on the level of economic development, climate conditions and historical regulation. One of the most common ways to cope-with waste is landfilling. Landfilling requires the use of extensive tracts of land and can have several environmental impacts on the land, atmosphere, hydrosphere, and biosphere. Another downside the landfills present is that even in the controlled ones the energy of the waste might be partially recovered, a complete utilization of the energy of the wastes is unfeasible. Thereupon, the European Union is encouraging landfill-dominant countries to find alternative waste management strategies. Incineration with energy recovery is a common effective option (Aracil et al., 2018). This is because incineration does not only require fewer space, but it also reduces considerably the volume of wastes (the solid

volume of the original waste is reduced by up to 90% and the solid mass by 80%–85%). In addition to obtaining energy simultaneously, avoiding CH_4 release, mitigating the contamination of water and contributing to a circular economy (Gu et al., 2019; Van Caneghem et al., 2019).

In Europe, in 2018, out of all the municipal waste treatment, nearly half of it was recycled (48.2%, including recycling as material and compost/digestion processes), and the remaining half was mainly either landfilled (24.1%) or incinerated with energy recovery (26.7%). It must be pointed out that in the past incineration without energy recovery was an alternative for municipal waste treatment. In the year 2007 up to 7.51% (out of the total treated waste) was incinerated without energy being recovered. But this percentage has decreased during these last years, becoming in 2018 only a 0.5% of the total waste treatment, due to the benefits presented when energy is recovered, thus, becoming a more attractive alternative.

Conversely, in Spain half of the municipal waste was landfilled (51%). The remaining was mostly recycled (34.8%, this percentage is divided in two different categories, including recycling-material and compost and digestion) and only a small percentage was incinerated with energy recovery (18.1%). Hence, if the situation of Europe is compared with the one of Spain in 2018, notable differences are seen. Nevertheless, the MSW treatment in Spain has not always been like the previously mentioned one, in fact, the situation of Spain has varied during the years.

Figure 1 represents the evolution of municipal waste treatment from 1995 to 2018 in kg per capita in Spain, where notable difference can be observed. In the year 1995 nearly all the MSW was landfilled. This started to change in the year 2000, when the amount of MSW raised considerably and the quantity landfilled did not increase. This was due to the great boost the recycling alternative experienced, either as a material or as compost form. Since then, the landfilling rate has dropped significantly, which was encouraged by the entrance into force of European regulations. Nevertheless, a large share of the municipal waste is still being landfilled. In the last decade, the amount of MSW has stabilized after it diminished noticeably in a period which corresponded to the Spanish crisis. In this picture, it can also be seen how the contribution of the energy recovery has doubled from 1995 to 2008.

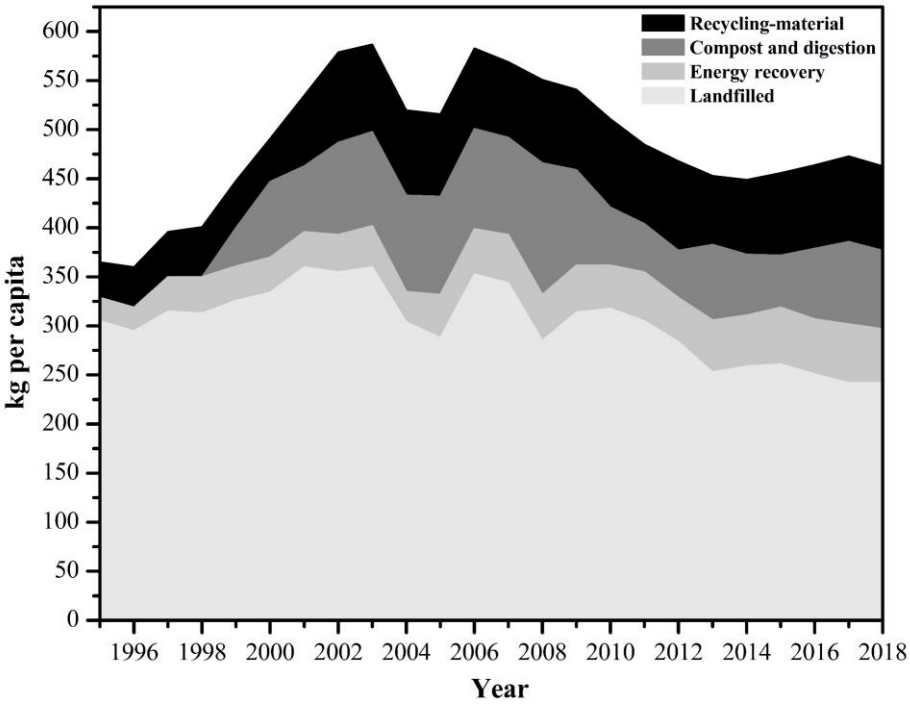

Figure 1: Municipal waste treatment in Spain from 1995 to 2018.

Regarding to Spain, it must be highlighted that Melilla and Balearic Islands are the ones that use incineration the most, in the case of Melilla 87.8% of the total treatment of municipal waste and in the case of Balearic Islands a 56.4%. Another fact to bear in mind is that although approximately half of the MSW generated is landfilled in Spain every year, landfill sites are more concentrated in the South, whereas incineration plants are mostly located in North (Aracil et al., 2018). This can be corroborated with the following example, based on the data of the Annual Report on Waste Generation and Management of 2018. In Andalusia none of the total municipal waste was incinerated while the 69.6% was landfilled; contrary in the Basque Country 25.9% of the total municipal waste was incinerated and 29.9% was landfilled.

In the Basque Country, more concretely in Biscay, it is found the Zabalgarbi incinerator. It consists of a combined-cycle gas plant technology constituting an innovative waste-to-energy plant, recording a net yield of 42% which is a remarkably high yield compared to that obtained in traditional energy recovery plants. The use of urban waste instead of fossil fuels and its highly efficient plant enable Zabalgarbi to deliver significant primary energy savings, as well as at the same time, reducing atmospheric CO_2 emissions per KWh generated (175% less than the emissions from a landfill).

Taking all this into account municipal solid waste incineration (MSWI) is reported to be a promising alternative to deal with the current situation, presenting advantages of high-efficiency, harmlessness, and resource utilization. However, some flue gas pollutants, including NO_X, SO_2, HCl, CO, volatile organic compounds (VOC) and dioxins, are often generated during the MSWI process. As well as some solid pollutants, such as particles and heavy metals, among others. To try to ensure the environmental security some emission limits exist and are presented in The Industrial Emission Directive (Directive 2010/75/EU). To meet these limits a flue gas clean line is necessary. Inside this clean line different ways to eliminate NO_X and PCDD/Fs exist. The attention of this study will focus on the simultaneous abatement of these two compounds using alternative catalysts.

1.1. TECHNOLOGY FOR THE REMOVAL OF NO_X

The generated NO_X are greenhouse gases. They are responsible of the acid rain and photochemical smog. They act as a precursor of both tropospheric ozone (O_3) and particulate, among other environmental issues, and cause several health problems (e.g. adverse respiratory effects) (Degraeuwe et al., 2016). The NO_X limit for waste incineration plants is presented in The Industrial Emission Directive, in the Annex VI, part 3. Daily average emission limit value for NO_X is 200 (mg/Nm^3). In MSW incineration plants, NO_X are mainly formed by the oxidation of the nitrogen found in the composition of the municipal waste, because the temperature of the reaction is not enough to oxidize the nitrogen of the atmosphere. In fact, thermal NO_X is only significantly formed at temperatures above 1300 °C (Neuwahl et al., 2019).

These nitrogen oxides are usually eliminated applying the selective non catalytic reduction (SNCR), because it is simple handling and cheap (Hwang et al., 2009). In this process NO_X are reduced in the combustion chamber by injecting a reductive agent, normally ammonia (which is another important greenhouse gas) or urea solution. The reactions occur at temperatures between 850 °C and 1000 °C. This is the strategy that uses the previously mentioned Zabalgarbi incinerator to eliminate the NO_X emissions. Nonetheless, this process is not very effective and needs high gas homogeneity and an excess of reductive agent in the chamber to reach more than 60-80% NO_X conversions (Neuwahl et al., 2019). As a result, high amount of unreacted NH_3 exits from the chamber, what is known as ammonia slip, and must be removed in the flue gas clean line before emitting the gas effluent to the environment.

Due to all this, the selective catalytic reduction (SCR) is a more interesting technology (Van Caneghem et al., 2019). The reaction occurs in a catalytic reactor (working between 150 ºC to 450 ºC), where the nitrogen oxides react with the ammonia and the oxygen present in the medium, forming nitrogen and water (Ec. 1.1). In this reaction other byproducts can be formed, so this formation has to be prevented. The commercial catalyst used in this reaction generally consists of the active phase, V_2O_5, supported on TiO_2. WO_3 and MoO_3 can be added as promoters, to improve the catalyst characteristics. Other substances have been studied, such as platinum, rhodium, and zeolites to form this catalyst. Due to poisoning, deposition, sintering and erosion, these catalysts usually present a limit lifetime of three to five years (Neuwahl et al., 2019). The SCR reaction achieves considerably higher efficiency and conversion compared to SNCR (typically a NO_X reduction rate of over 90%). Comparing the emission levels of NO_X and NH_3 associated with the SNCR (being the annual maximum of half-hourly NO_X averages 155-300 mg/Nm^3 and of NH_3 5-60 mg/Nm^3) with the ones linked to the SCR (5-200 mg/Nm^3 for NO_X and 3-30 mg/Nm^3 for NH_3) actual improvements can be observed.

$$4NO + 4NH_3 + O_2 \rightarrow 4N_2 + 6H_2 \qquad (1.1)$$

1.2. TECHNOLOGY FOR THE REMOVAL OF PCDD/Fs

Polychlorinated dibenzo-p-dioxins (PCDDs) and polychlorinated dibenzo-p-furans (PCDFs), also referred to as PCDD/Fs, belong to the group of persistent aromatic compounds. The common chemical structure of PCDDs is composed by two aromatic rings bounded through a pair of oxygen atoms, whereas only one characterized PCDFs structure. PCDD/Fs are a great threat to the ecological environment and human health, due to their persistence, toxicity, and potential for bioaccumulation (Li et al., 2021b). They are a potent carcinogen and act like an extremely persistent synthetic hormone, perturbing important physiological signalling systems.

Among other important problems, they alter cell development (Schecter and Gasiewich 2003). They are formed unintentionally during various industrial thermal processes, such as in power generation processes, in metallurgical facilities, and in municipal solid waste incineration plants (Liu et al., 2015). The Industrial Emission Directive establishes that the average emission limit value for dioxins and furans is 0.1 (ng/Nm^3) over a sampling period of a minimum of 6 hours and a maximum of 8 hours.

The PCDD/Fs found in the crude flue-gas of waste incineration plants are the result of recombination reactions of carbon, oxygen, and chlorine. Suitable precursor substances (e.g. from chlorophenols) can also react to form dioxins and furans. Some transition metal compounds (e.g. copper compounds) can act as catalysts for the formation of PCDD/Fs, this is what is known as novo synthesis (200-450 ºC) (Neuwahl et al., 2019). On the one hand, formation of dioxins can be prevented before they are created (that is source control and process control), what would be the preferable option. On the other hand, when they have been already created, they must be removed (end treatment).

Source control is a technique that can weaken the formation of PCDD/Fs precursors by optimizing combustion conditions and improving furnace type structure (such as removing the plastic before the combustion), thereby reducing PCDD/Fs emissions. However, this method cannot prevent the de novo synthesis of PCDD/Fs on the fly ash surface during the cooling process. Differently, the process control, featured by adding inhibitors to suppress the formation of PCDD/Fs, has been extensively studied and applied in MSWI due to the low cost and high efficiency. The inhibitors used include the N-containing inhibitors, S-containing inhibitors, and alkaline inhibitors. An example of this are the successful results obtained adding thiourea in a MSW incineration plant (Zhan et al., 2016; Qian et al., 2021).

Regarding to the end treatment, the most common system is activated carbon adsorption, coupled with bag filter. Adsorption on activated carbon can be accomplished in carbon fibers, packed beds, entrained flow techniques, with the injection of this adsorbent or in moving beds. Other less common materials such as hydrophobic zeolites, sepiolite or carbon nanotubes are occasionally used. Another alternative for the PCDD/Fs abatement is the wet scrubbing, either with carbon-impregnated materials or carbon slurries (Finocchio et al., 2006; Gallastegi-Villa et al., 2020). Nevertheless, technical challenges are facing these strategies, because PCDD/Fs are just transferred from the gas phase to the solid or liquid phase. Then the solid phase generated needs to be treated or landfilled. Due to this drawback, the use of catalytic filter bags becomes an interesting alternative, presenting the opportunity of eliminating the PCDD/Fs in the filter itself, rather than only separating them. Besides, it is not only capable of eliminating the PCDD/Fs present in particulate materials, but also the ones present in the gas phase. Destruction efficiencies of above 99% are reported at a MSWI with the use of catalytic filters (Neuwahl et al., 2019). This system has already been developed in different MSW incinerator plants; as an example, IVRO municipal waste incinerator, which is located in Belgium, adopted catalytic bag filters (Bonte et al., 2002).

Catalytic destruction units (e.g. monolith reactors), through catalytic total oxidation reaction, make possible to destroy the PCDD/Fs forming CO_2, HCl and water (Ec. 1.2). In general, catalytic processes are applied after initial dedusting. The dust that is removed at the pre-dedusting stage will carry with it the adsorbed PCDD/Fs, which may be the majority. Although high cost and high moisture and dust content in the flue gas might limit the application of this technique, catalytic destruction is an efficient way to eliminate PCDD/Fs, used in many MSWI plants (Qian et al., 2021). Research has been done over the years trying to find the optimum catalyst. In these previous investigations, an outstanding discovery was made. It was seen that

there are catalysts that are active in both oxidation and SCR reaction (Lin et al., 2020). This is the case of the study developed by Wang et al. (2003) where the emissions of four sinter plants in Taiwan were compared and they found that the dioxin emissions of the plants where tail gas was treated with SCR reactors were lower than those without SCR (Finocchio et al., 2006). This discovery leads to a great opportunity, making it possible to eliminate these two compounds in a unique step.

$$C_{12}H_nCl_{8-n}O_2 + (9+0.5n)O_2 \rightarrow (n-4)H_2O + 12CO_2 + (8-n)HCl \qquad (1.2)$$

1.3. SIMULTANEOUS REMOVAL OF NO_X AND PCDD/Fs

The removal of NO_X and PCDD/Fs can be achieved in the same catalytic reactor, where at the same time the PCDD/Fs are oxidized, and the nitrogen oxides are reduced. There are few studies about this strategy either in industrial scale or laboratory scale. For instance, Goemans et al. (2004) developed a study of this simultaneous abatement in a Belgian incinerator plant. In this study a PCDD/Fs destruction of a 99% was achieved (values of 0.001 ng TEQ/Nm^3 were obtained, less than 1% of the norm), and at the same time, NO_X were reduced by 90%.

Regarding the lab-scale studies, not a wide variety of them exist which analysed the simultaneous abatement of these two substances, due to the presented complexity, focusing the majority of them on a unique removal reaction. An example of these lab-scale investigations is the one carried out by Finocchio et al. (2006) in which the data reported reaffirm that the combined NO_X and PCDD/Fs abatement technologies are effective techniques for the purification of waste gases from MSWI, fulfilling largely the limit of PCDD/Fs. On the other hand, Liu et al. (2015) developed the study with a pilot plant, focusing the attention on the effect of the temperature. A temperature range between 220-300 ºC was analysed and removal efficiencies of PCDD/Fs and NO_X increased along with the rise of the temperature, revealing that higher temperature facilitates the catalytic oxidation of PCDD/Fs and the selective catalytic reduction of NO_X. The test at 300 ºC gave the highest removal efficiencies of PCDD/Fs and NO_X being 97.24% and 90.3%, respectively.

In the University of the Basque Country (UPV/EHU), a research line about this subject is being carried out by the Chemical Technologies for Environmental Sustainability (TQSA) group, inside the Chemical Engineering department. In order to achieve this purpose, an experimental equipment was developed, which simulates a feed gas to the catalytic reactor in tail-end configuration. To begin this study, it was analysed the simultaneous abatement of PCDD/Fs and NO_X with a VO_X/TiO_2 catalyst. It was concluded that the removal of NO_X and PCDD/Fs could be achieved using this catalyst and that this simultaneous abatement did not occur in an independent way (therefore it is important to study the two reactions both together). The major problem reported was that NO reduction occurred at lower temperature than PCDD/FS oxidation. PCDD/Fs conversion showed typical S-shaped form, because of the exponential dependence of the reaction kinetic constant with temperature, described by the Arrhenius equation, rising its conversion until ca. 500 ºC (to achieve half of the PCDD/Fs conversion ca. 250 ºC were needed). NO conversion also followed the same shape until 190 °C temperature, in which a maximum conversion was reached. At higher temperature, contrastingly, NO conversion decreased. Therefore, the complete removal of these two compounds, using this catalyst, is impossible. Hence, the use of alternative catalyst was suggested. Further investigation was done taking these results into account and it was concluded that an active phase based on manganese and cerium, which are transitional metals, was a good choice to create alternative catalysts for this simultaneous abatement reaction (Gallastegi-Villa 2016).

Manganese-based catalysts have good redox properties (due to the rich variable valence states), promising activity at low temperatures, and excellent oxygen migration ability. These properties are beneficial for oxidation of NO to NO_2, and lead to relatively high conversion of NO_X at low temperatures. The mentioned properties have also positive effects for the application of this type of catalysts in the oxidation of chlorinated organic compounds, which can be confirmed by the study made by Santos et al. (2010). However, the low N_2 selectivity, poor H_2O resistance, and narrow operating temperature window of manganese-based catalysts require further improvements. On the other hand, ceria (CeO_2) has been widely used to eliminate NO_X owing to its good redox properties and high oxygen storage-release capacity associated with oxygen vacancies in the material and the Ce^{4+}/Ce^{3+} redox couple. It has also been reported that CeO_2 can promote adsorption of NO_X, provide stronger Brønsted acidic sites, enhance oxidation of NO to NO_2, and improve the water and sulphur resistance of catalysts, which would be particularly beneficial for the NH_3-SCR model reaction. Therefore, a combination of manganese oxide (MnO_X) and CeO_2 to form MnO_X-CeO_2 catalysts could improve the materials catalytic performance for the SCR of NO_X (Few studies exist corroborating this idea, such as the one developed by Yao et al. in 2017) and PCDD/Fs oxidation reaction (This idea can be reflected in the study made by Wang et al. in 2008).

It has been widely reported that the physicochemical properties and catalytic performance of catalysts are highly dependent on their preparation methods and active phase content. Also, the content of each metal of the active phase is another key factor. In previous investigations carried out by the mentioned TQSA's investigation line, it was concluded that the best results were obtained using co-precipitation method. This was because the catalyst prepared with this method where the ones presenting the highest NO_X and PCDD/Fs conversions. With co-precipitation method, Mn incorporates to the CeO_2 structure, creating a solid solution. This solid solution enhances the redox properties through the generation of oxygen vacancies, which improve oxygen mobility. Moreover, tests corroborated the better activity of catalysts prepared by co-precipitation, with increased NO and o-DCB conversion at low temperature. Inside the co-precipitation catalysts, the sample with 85% Mn 15% Ce molar composition showed the best catalytic behaviour for the process (even NO_X reduction and PCDD/Fs oxidation were not totally selective, which leaded to the generation of by-products). Thence, this method and this composition has been used for all the prepared catalysts.

Another key factor that may determine the catalyst is the support. The support can perform a crucial role when it comes to thermal stability, use of the active phase, plus stability and dispersion of the active phase. Consequently, the support can be an interesting component to consider as it could improve the MnO_X-CeO_2 catalysts. A wide bibliographic search has been accomplished and four different supports have been selected to be analysed in this study. On the one hand, the alumina is the most used commercial support. In the SCR reactions alumina with incorporated transition metal species is largely used. The crystalline structure of Al_2O_3 is highly defective and, therefore, its inherent surface and structural properties facilitate the dispersion of transition metal species on the support (Gonçalves et al., 2021). Another interesting fact is that Al_2O_3 can provide Brønsted acids, which may be interesting for the abatement reaction (Xu et al., 2021).

On the other hand, titanium dioxide has been used successfully in much research. Titanium dioxide is highly porous and has a large surface area, being of great prominence to boost the catalytic performance, is extensively used in SCR reactions. It also has high chemical stability and high ion-exchange capacity (Boningari et al., 2015). The last analysed support are the zeolites. Two different zeolites have been studied, H-ZSM5 zeolite and H-Beta zeolite. These microporous aluminosilicates possess acidic properties, in addition to an ordered channel

structure and high hydrothermal stability. Besides, the H-ZSM5 is thought to improve the active phase, preventing its drawbacks, as it has been reported to reduce the formation of N_2O (Fermanelli et al., 2021).

In this study the introduced four supports (Al_2O_3, TiO_2, H-ZSM5 and H-Beta) are going to be analysed with three different active phase loads (5%, 10% and 20%, respectively, referring to the manganese content in regard to the total catalyst grams) as an attempt to improve the alternative catalysts for the simultaneous removal of NO_X and PCDD/Fs.

2. OBJECTIVES

In line with the Chemical Technologies for Environmental Sustainability group research field, the main objective of this research is to analyse the performance of alternative catalyst composition based on MnO_X-CeO_2 supported on four high surface materials, namely, Al_2O_3, TiO_2, H-ZSM5 and H-Beta. It includes analysing the effect of MnO_X-CeO_2 load (5%, 10% and 20%). The following milestones have been defined to reach this objective.

-Prepare different catalysts using co-precipitation method. Three different active phase loads 5%, 10% and 20% have been added to each support. These percentages are referred to the manganese active metal out of the total catalyst grams, being 85Mn-15Ce the optimal molar ratio.

-Characterize the catalysts in order to determine the physico-chemical characteristics that play an important role in the catalyst activity. These characteristics are crystallinity, acidity, redox and textural properties.

-Test the catalytic activity, selectivity and durability of prepared catalysts in a lab-scale reactor set-up, which allows performing both reactions, NO_X selective reduction and o- DCB oxidation, simultaneously.

-Analyse kinetic and characterization data in order to conclude the effect of supporting MnO_X-CeO_2 on the simultaneous catalytic abatement of NO_X and o-DCB, and also to determine the effect of MnO_X-CeO_2 content.

3. MATERIALS AND METHODS

3.1. CATALYSTS PREPARATION

Mn–Ce composite oxide catalysts (MnO_X-CeO_2, 85Mn-15Ce molar ratio) supported on Al_2O_3, TiO_2, H-ZSM5 and H-Beta were prepared by co-precipitation method. Firstly, all the supports were calcinated at 550 ºC with a heating ramp of 1 ºC/min for three hours in order to provide thermal stability. In the case of the zeolites the calcination was also conducted to obtain their protonic form (H-ZSM5 y H-Beta), since they were initially in their ammonium one (NH_4-ZSM5 y NH_4-Beta). Once the support had been calcinated, its suspension was prepared. In each case, certain mass of the support was suspended in 100 mL distilled water (in order to maintain constant conditions) and the corresponding suspension was stirred with a magnetic stirrer at room temperature. In the case of the alumina, the pH of the suspension was adjusted to ca. five using nitric acid (0.1 M), as the alumina, unlike the rest, promotes a basic suspension in water. This procedure allows the start of the precipitation process from the same acid conditions, as well as avoiding the precipitation of metal cations.

In addition, the proper amounts of manganese nitrate ($Mn(NO_3)_2{\cdot}4H_2O$) and ceria nitrate ($Ce(NO_3)_3{\cdot}6H_2O$) were weighed and dissolved in distilled water. In this way, a 0.46 M $Mn(NO_3)_2{\cdot}4H_2O$ solution and a 0.37 M $Ce(NO_3)_3{\cdot}6H_2O$ solution were prepared. The prepared solutions were stirred with a magnetic stirrer until homogeneity was reached. Subsequently, the prepared precursors solutions and the suspension of the support were mixed. In order to promote the precipitation of the metal cations, the pH was risen until nine, adding ammonia carbonate ($H_2NCOONH_4$) drop by drop. Once this pH was obtained, it was left for two hours ageing. The resulting precipitate was filtered and washed several times with distilled water. Next, the precipitate was dried in an oven over the night at 100 ºC. Lastly, the dried samples were calcinated with the muffle furnace in air at 500 ºC for three hours with a heating ramp of 1 ºC/min. To finish, the catalysts were pelleted, powdered, and sieved to 0.3-0.5 mm, as it has been demonstrated that at this size the controlling step is the chemical reaction.

The mentioned procedure was followed to prepare three different catalysts for every single support (Al_2O_3, TiO_2, H-ZSM5 and H-Beta). These three catalysts differ in the content of active phase. 5%, 10% and 20% active phase loads catalysts have been prepared (the mentioned percentages are referring to the manganese content, regarding the total catalyst grams with an 85Mn-15Ce molar ratio).

3.2. CHARACTERIZATION OF THE CATALYSTS

3.2.1. X-Ray Fluorescence Spectrometry

X-Ray Fluorescence Spectrometry (XRF) characterization technique has been accomplished to analyse the chemical composition of the catalysts. XRF is a semiquantitative analysis in which the samples are in powder form and are located with mylar in a sample holder, which is submitted to a vacuum atmosphere for the analysis. The analysis has been conducted in a sequential X-ray fluorescence spectrometer (PANalytical, AXIOS model) by the dispersion of wavelengths (WDXFR). The spectrometer is equipped with a Rh tube and three detectors. To carry on the analysis a standardless software is used. The software is based on the measurement of a group of scans, with different crystal analysers, which determine the presence of different elements.

3.2.2. Scanning Electron Microscopy

Scanning Electron Microscopy (SEM) characterization technique has been employed to obtain images of the catalysts. SEM creates an image by detecting reflected or knocked-off electrons, providing information on the surface of the sample and its composition. This characterization technique has been conducted by the University of the Basque Country's general analysis services (SGIKER).

3.2.3. Scanning Transmission Electron Microscopy-High Angle Annular Dark Field

Scanning Transmission Electron Microscopy-High Angle Annular Dark Field (STEM-HAADF) characterization technique has been carried out to obtain spatially resolved elemental analysis of the samples. A scanning transmission electron microscopy (STEM) is a type of transmission electron microscopy (TEM). TEM uses transmitted electrons to create an image. The TEM apparatus is connected to a detector for Energy Dispersive X-Ray Spectroscopy (EDXS) elemental mapping. This characterization technique has been conducted by the Institute of Nanoscience and Materials of Aragon (INMA).

3.2.4. Physical adsorption of nitrogen

Surface area and pore characteristics have been studied with N_2-physisorption at 77 K and at sub-atmospheric pressures. To accomplish this nondestructive technique two different equipment of Micromeritics brand are used: TriStar II is used for mesoporous materials and ASAP 2020 is used for microporous materials. The latter offers higher accuracy at low relative pressure, at which information of the micropores is obtained. The same procedure is followed in the two cases. Firstly, a pretreatment is done. In the case of the microporous materials the pretreatment is conducted in a vacuum atmosphere (< 1 Pa), rising the temperature (10 ºC/min) up to 400 ºC and keeping this temperature for 10 hours. In the case of the mesoporous materials, it is achieved at atmospheric pressure, under a constant N_2 stream, heating up 10 ºC/min the sample to 350 ºC and maintaining this temperature for 5 hours. In this way, all the possible molecules adsorbed in the surface (moisture, oxygen, carbon dioxide and so on) are removed. Afterwards,-the analysis is performed adding certain volumes of N_2. N_2 adsorbs on the surface of the catalyst and once the equilibrium has been achieved, the resultant relative pressure is recorded. The succession of all the recorded data allows the representation of the adsorption branch. The representation of the N_2 adsorbed volume at equilibrium conditions versus the relative pressure of the adsorbed gas (P/P_0, where P_0 is the vapor pressure of the adsorbed gas in the temperature of measurement) is known as isotherm. To obtain the desorption branch, this same process is repeated but now eliminating fixed volumes of N_2.

The isotherm obtained from these adsorption measurements provides information on the surface area, pore volume, and pore size distribution. The classical pore size model developed by Barrett, Joyner and Halenda (BJH), which is based on the Kelvin equation and corrected for multi-layer adsorption, is used for calculations of the pore size distribution over the mesopore, hence, this model is used for the Al_2O_3 and TiO_2. The Gurvitsch method is applied for micropore pore volume calculations, i.e., for zeolites. The Gurvitsch method represents a simple model, independent of pore geometry, to estimate the total pore volume. This estimation is made from the amount of adsorbate corresponding to the inflection point of the high pressure plateau when represented the adsorbed volume vs. time (López-Fonseca, 2001). Additionally, Brunauer, Emmett and Teller proposed five different isotherm models depending on the characteristics of each solid and the adjustment to the Brunauer, Emmett and Teller equation, known as BET. This equation is used for the calculation of the superficial area. Anyway, one

must be aware of the fact that physical phenomena like the tensile strength effect, adsorbate phase transitions, and monolayer formation in combined micro and mesoporous materials frequently lead to extra contributions in the adsorption isotherm (Groen et al., 2003).

3.2.5. X-Ray Diffraction

X-Ray Diffraction (XRD) technique, conducted with Philips PW 1710 diffractometer, has been used to provide information on crystallographic structures. It operates with the copper radiation Kα (λ=1.54106 Å) and a filter of nickel. XRD is commonly used to determine the bulk structure and composition of heterogeneous catalysts providing information about the existing phases, preferred crystal orientations (texture), and other structural parameters, such as average grain size, crystallinity, strain, and crystal defects.

XRD peaks are produced by constructive interference of a monochromatic beam of X-rays scattered at specific angles from each set of lattice planes in a sample. In this case, samples have been scanned between 10° and 80° (2Θ) with 0.02°/s sampling interval. Because most catalysts are in the form of polycrystalline powders, the XRD analysis is typically limited to the identification of specific lattice planes that produce peaks at their corresponding angular positions 2Θ, determined by Bragg's law. In spite of this limitation, the characteristic patterns associated with individual solids make XRD quite useful for the identification of the bulk crystalline components of solid catalysts. The peak intensities are determined by the atomic positions within the lattice planes. Consequently, the XRD pattern is the fingerprint of periodic atomic arrangements in a given material. Powder Diffraction File established by the International Centre for Diffraction Data offers a wide variety of diffractograms for different phases. These diffractograms have been used for the identification of the prepared catalysts crystal phases comparing them with the experimentally obtained ones (Ma and Zaera 2016).

If considered an X-ray reflection on N lattice planes of spacing d the thickness of the crystallite $L=Nd$ in the direction perpendicular to the reflecting planes can be obtained from the width Δ(2Θ) of the reflection corrected for instrumental broadening with the Scherrer equation:

$$L=\frac{k\lambda}{\Delta(2\Theta)\cos\Theta_0} \qquad (3.1)$$

where λ is the wavelength, and Θ_0 is the Bragg's angle at line maximum. The constant k depends upon several factors, including the way Δ(2Θ) is measured and the shape of crystallites (Anderson and Boudart, 1984). Equation (3) is limited to particles larger than 3-4 nm, since the ones below this size are practically transparent to X rays.

3.2.6. NH_3-Temperature Programmed Desorption

NH_3-Temperature Programmed Desorption (NH_3-TPD) technique has been performed to analyse the acidic properties of the prepared catalysts. This technique links the ammonia desorption temperature with the acidity. NH_3 has relatively strong basicity, thus, it adsorbs on all acid sites. However, the temperature at which NH_3 desorbs depends on the acid strength of these sites. Micromeritics AutoChem II has been used to conduct this characterization. Firstly, a pretreatment is done. 50 cm^3/min of a 5% O_2/He stream are passed through the sample at 500 ºC for 45 minutes, with a heating ramp of 10 ºC/min, in order to remove any absorbed species from the surface. Then it is cooled down to 40 ºC, temperature at which the sample is completely saturated with ammonia by passing through a flow of 130 cm^3/min 1% NH_3/He for one hour. Once the saturation is completed, physisorbed or weakly adsorbed NH_3 is removed

passing through a flow of He (130 cm^3/min). Subsequently, temperature is risen up to 500 ºC at a rate of 10 ºC/min, in order to desorb the chemically adsorbed NH_3 passing He.

A thermal conductivity detector (TCD) is used to measure the desorbed NH_3. TCD works by having two parallel tubes both containing gas and heating coils. One tube holds a reference gas and the sample to be tested is passed through the other. The gases are examined by comparing the heat loss rate from the heating coils into the gas. Total acidity is calculated from the time integration of the total desorbed ammonia.

Given the surface oxygen the catalysts have, NH_3 may react with these species forming nitrogen oxides. For the purpose of studying the formation of these compounds, the composition of the outlet stream of the experiment is analysed with a mass spectrometer.

3.2.7. H_2-Temperature Programmed Reduction

H_2-Temperature Programmed Reduction (H_2-TPR) has been carried out to study the reducibility (redox properties) of the prepared catalysts. AutoChem II is used to perform this analysis. To begin, the sample is pretreated with 50 cm^3/min of a 5% O_2/He stream at 500 ºC for 45 minutes. The sample is heated at a rate of 10 ºC/min. Thereafter, the sample is cooled to 40 ºC. Temperature is risen anew (10 ºC/min) up to 950 ºC and kept constant 30 minutes in a 50 cm^3/min continuous stream of 5% H_2/Ar. This is made in order to reduce the catalyst. H_2 is the most used reductive agent due to its high reductive power and simplicity. In this technique the consumption of H_2 is measured with a TCD. Water is going to be formed while the catalyst reduces. This water can affect the measurement of the TCD, so it has to be condensed prior to the stream reaches the detector; hence, the stream exiting the reactor is passed through a cold trap.

The integration of the flow rate of the reducing agent used versus time reveals the reduction capacity of the catalyst. Furthermore, the temperature at which the reduction takes place reflects the reduction ability (reducibility) of the sample.

3.3. EXPERIMENTAL EQUIPMENT FOR THE SIMULTANEOUS REMOVAL OF NO_x AND PCDD/Fs

The lab-scale experimental set-up, designed by the Chemical Technologies for Environmental Sustainability group, allows to perform simultaneously the NH_3-SCR of NO_X and the catalytic oxidation of o-DCB (Ec. 1.1 and Ec. 1.2). Selectivity, activity, and stability of the prepared catalysts are analysed in similar conditions to the ones of a MSWI. The flow diagram of the experimental equipment is represented in Figure 2. It consists of three fundamental sections: feeding, reaction and analysis sections. The whole experimental set-up is made of AISI-316 stainless steel to deal with corrosion and avoid o-DCB adsorption.

The equipment allows to operate in a quasi-automatic mode and allows to control and monitor the operating variables (the flow of each of the reagents, their concentration, reaction temperature, reaction pressure and the heating of the thermally insulated areas) as well as the opening and closing of the process valves. It also allows to monitor the concentration of the products. A PLC (Programmable Logic Controller) connected to the analysers, mass flow controllers, and to a computer (which has a specific software) makes this possible.

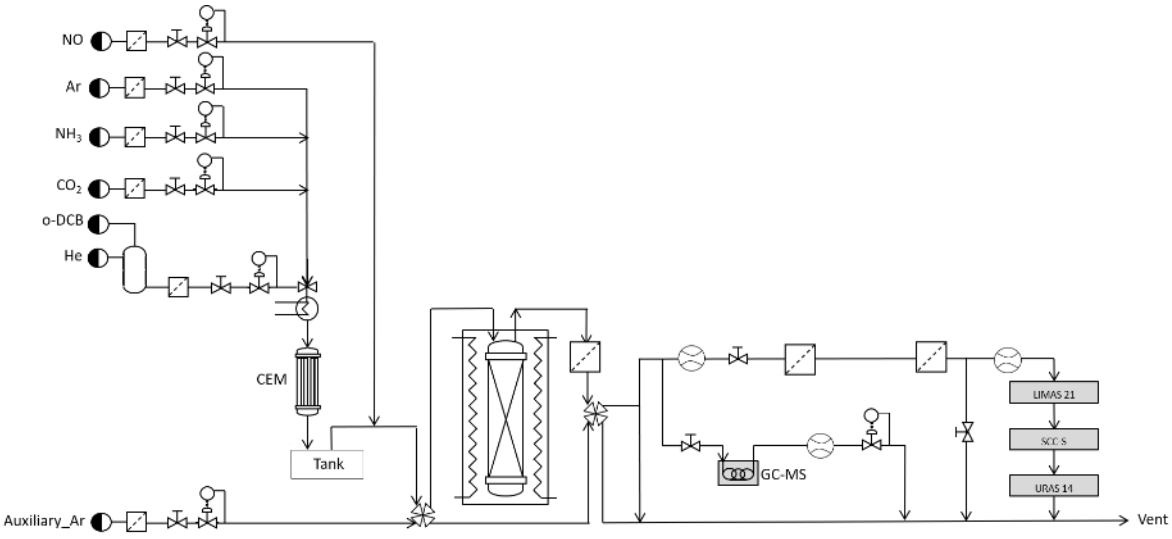

Figure 2: Flow diagram of the experimental set-up.

3.3.1. Feeding system

The simulated feeding stream has the composition presented in Table 1. The composition is slightly different from the one obtained in a MSWI. Firstly, working with PCDD/Fs in lab-scale is impracticable, owing to their high toxicity, handling difficulties and no commercial availability. Therefore, a less harmful compound with a similar structure is utilized, 1,2-dichlorobenzene (o-DCB), which consists of a benzene ring with two chlorine atoms. Secondly, air is substituted by argon since the presence of N_2 would not allow to analyse the selectivity of the SCR reaction. Thirdly, even though CO (< 5%) and CO_2 (6-8%) are present in the outlet gas stream of MSWI, they are not included because they have been previously checked not to significantly affect NO reduction nor o-DCB oxidation. Besides, their excess would make it difficult to analyse the selectivity towards them in o-DCB oxidation.

Table 1: Nominal concentration values of the stream entering the reactor.

Compound	Unit	Concentration
NO	ppm	300
NH_3	ppm	300
o-DCB	ppm	100
O_2	%	10
Ar	Balance	

The feeding stream is obtained synthetically from pure compounds. Gas flows (Ar, O_2, NO and NH_3) are regulated by Bronkhorst, F-201CV gas mass flow controllers, whereas o-DCB liquid stream is dosed by a Bronkhorst μ-Flow L01-AGD-19-0-20S mass flow controller. All of them are preceded by a filter (5-9 μm) to avoid the entering of particles.

To ensure complete evaporation of o-DCB, its dosing pipe is wrapped by a flexible heating cord, and to favor the homogenous mixture with the gas stream, a mixing valve, and a controlled-evaporator-mixer (Bronkhorst, W-102A-111-K) are disposed. In addition, in order to buffer potential oscillations of every component feed concentration and to favour complete homogeneity, the stream is carried through a 25 L tank.

Parallel to the feed line, there is an auxiliary argon line for diverse operations: cleaning the pipeline, drying catalyst bed, calibration operations of the analysers, etc. This line is also

equipped with a filter and a mass flow controller. The auxiliary argon line and the feeding stream enter a four-port pneumatic valve. This valve allows to carry the feeding stream to the reactor, and the auxiliary argon to by-pass, or vice versa.

3.3.2. Reaction system

The reaction system is composed of a U-shaped tubular quartz reactor located in the middle of a convective-flow oven, which allows an accurate temperature maintenance and the programming of heating ramps. To ensure appropriate fluid-dynamic conditions and absence of diffusional control, the reactor has a defined inner diameter of 13.6 mm. The quartz tube, in one of its upper branches (inlet branch), has a stainless steel connection through which the thermocouple can be located, and the reaction gas can be fed through the other. The gas mixture flows down the tube meanwhile it is heated up until it reaches the catalytic bed. The catalytic bed is positioned over quartz wool, 15 mm above the inferior part of the reactor (to ensure absence of the longitudinal temperature gradient and better temperature control). The gases flow through the catalyst in a downward direction and the gaseous products leave the quartz tube on the other branch (outlet branch). The outlet stream of the reactor and the bypass line end up in a second four-port valve which allows sending the reaction outlet stream to analysis and the bypass stream to vent, or the other way round.

The reaction conditions are given in Table 2, which have been set up to make the chemical reaction stage the slowest stage of the whole physicochemical process, in order to work under intrinsic kinetic conditions, eluding diffusional controls.

Table 2: Reaction conditions.

Variable	Unit	Value
Volumetric flow	L_N/min	2
Particle size	mm	0.3-0.5
Catalyst weight	g	1.5
Space velocity	h^{-1}	40000
Linear velocity of the gas flow	m/s	13.77
Pressure	atm	1.8

3.3.3. Analysis system

The analysis system is composed of different analysers which enable the quantification of the reagents before and after the reaction, as well as the quantification of the reaction products.

The outlet stream of the reactor sent to analysis is divided in two. One part of stream goes to the chlorinated organic compounds analysis and the other goes to the analysis of non-organic compounds. Right before the non-organic compounds analysis systems the excess gas flow is sent to vent.

3.3.3.1. Analysis of chlorinated organic compounds

A gas chromatograph equipped with a mass selective detector (GC-MS, Agilent Technologies 7890-5975C) is utilized for the measurement of o-DCB and other chlorinated organic by-products which may be formed during the oxidation. This analytical technique makes possible to separate the components of a blend according to different velocities at which they move through a stationary phase when transported by a mobile phase. According to the composition

of the exhaust gas stream, a HP-COV column is used as stationary phase. He is used as mobile phase (carrier).

The sample flows through a loop connected to a 6-way valve. At the time of injection, the valve connections change position and the sample previously retained in the loop is drawn into the injector by the carrier. To keep the same amount of moles introduced into the injector, there is a pressure controller which maintains the pressure at the outlet of the chromatograph constant.

Table 3 shows the established method for the chromatographic analysis. The quantification of the chromatograms is attained using an equation obtained after the calibration with different liquid standards, varying the injection volume and split ratio in order to change the amount of analyte injected into the chromatographic column.

Table 3: Description of the chromatographic method.

Parameter	**Value**
Column	HP-VOC, 30 m × 250 μm × 0.2 μm
Mobile phase	He
Injected volume	0.25 mL
Injector temperature	150 ºC
Split ratio	1/30
Column flow	1 mL/min
Column pressure	8.232 psi
Oven	70 ºC (2 min), 60 ºC/min up to 200 ºC, 200 ºC (0.5 min)

3.3.3.2. Analysis of non-chlorinated inorganic compounds

Two different analysers of ABB, placed in series, are used to quantify the concentration of the measured compounds. Between them an ABB SCC-S Sample Gas Feed Unit is placed, in order to condensate the water which might be formed, with its membrane filter/condensate monitor.

For CO, CO_2 and N_2O an URAS 14 analyser is utilized. Its measurement principle is the NDIR technique (Non-Dispersive InfraRed Analysis). The measurement is based on resonance absorption of gas-specific vibration-rotation bands of gas molecules with differing atoms in the median infrared spectrum at wavelengths between 2.8 and 8 μm. The individual gases to be measured are identified by their specific absorption bands. Each gas has a unique absorption spectrum (fingerprint).

On the other hand, for the quantification of the concentration of NO and NO_2 a LIMAS 11 analyser is used. The measurement is based on the specific emission absorption of each component within the ultraviolet wavelength range (200-500 nm). Emission absorption is produced when the molecule transitions to a higher electron state in which various oscillation states are assumed. This creates an entire absorption band system.

3.4. REACTION PROCEDURE

The reaction protocol consists of four different stages:

I) In a first stage, the catalytic bed is treated for one hour with a 1.5 L_N/min argon stream at 200 ºC, in order to remove the possible molecules adsorbed in the surface. The argon stream is directed to vent.

II) Simultaneously, the feeding stream is prepared and stabilized, by flowing through the reactor by-pass.

III) When the feeding stream is stabilized, it is sent to analysis with the positioning of the second four-port valve, leading to the concentration measurement.

IV) In parallel, after the cleaning pretreatment the reactor temperature is diminished down to 75 ºC, temperature at which the reaction experiment starts. The reaction is initiated by concurrently switching the position of the two pneumatic four-way valves, making the feeding stream flow through the reactor and through the analysis system. The temperature of the reaction is increased until 500 ºC, with a heating ramp of 1.5 ºC/min.

The catalytic performance is measured in terms of NO and o-DCB conversions, which are calculated with the following general equation, considering the concentration of each compound at the entrance of the reactor (C_{A0}) and at the outlet (C_A):

$$x_A = \frac{C_{A0} - C_A}{C_{A0}} \cdot 100 \qquad (3.2)$$

4. RESULTS

4.1. CATALYST CHARACTERIZATION

4.1.1. XRF

The Mn-Ce ratios have been calculated from the bulk chemical compositions and are listed in Table 4. As it can be observed, expected molar compositions have been obtained, which means that catalysts have been successfully prepared, with the effective deposition of the metals. In the case of the zeolites, Table 4 also shows their SiO_2/Al_2O_3 ratios. These ratios have been calculated to corroborate their nominal values provided by the supplier (50 for the H-ZSM5 and 25 for the H-Beta). A MnO_2-CeO_2 distribution (86.69 ± 0.76-13.58 ± 0.73) close to the desired distribution (85-15) has been achieved in all samples.

Table 4: Molar composition of the supported catalysts.

Sample	**Molar composition of the active phase (%)**							
	Al_2O_3		**TiO_2**		**H-ZSM5**		**H-Beta**	
	Mn	Ce	Mn	Ce	Mn	Ce	Mn	Ce
5% MnO_X-CeO_2	86.58	13.42	86.10	13.90	86.89	13.11	85.36	14.64
10% MnO_X-CeO_2	86.06	13.94	85.44	14.56	86.83	13.17	87.31	12.69
20% MnO_X-CeO_2	86.66	13.34	85.64	14.36	87.73	12.27	86.34	13.66
			SiO_2/Al_2O_3		54.68		25.11	

4.1.2. SEM

Morphological analysis of the catalysts has been done with SEM images. Figure 3 presents SEM images for the bare supports (Figure 3 first row) and for the 20% MnO_X-CeO_2 load supported catalysts (Figure 3 second row). It can be seen that in all cases the surface morphologies of the supports and the prepared catalysts are different. The alumina support seems to present a structure with low crystallinity and its surface is smoother than the surface when the active phase is supported (Zhang et al., 2021). Their particle size is reduced when the active phase is supported. This happens in the case of the H-Beta zeolite as well, suggesting that the load of active phase makes the support to split into smaller particles.

TiO_2 sample consists of highly agglomerated nanoparticles which have irregular spherical shapes (El Mragui et al., 2021). SEM image of the H-ZSM5 is similar to the one of the titania consisting of several spherical structures (Li et al., 2021a). In these two cases the size of the particles is increased when the active phase is supported, suggesting that the active phase has been deposited over the nanoparticles of the supports creating bigger ones.

Interestingly, in the four supported catalysts the same overall consequences are observed. The active phase promotes homogeneous regular spherical shapes of similar size independently to which the support is, although in zeolites apart from these spherical particles micrometer size particles are seen. This could be because in the active phase load catalyst, the active phase has only been loaded in some particles of the support, remaining the rest just as found in the bare support.

These all indicates that, on the one hand, a good deposition of the active phase has been achieved with the co-precipitation method, and that the morphology of the prepared catalysts would not be a key factor in the catalysts activity results as they all present a similar one.

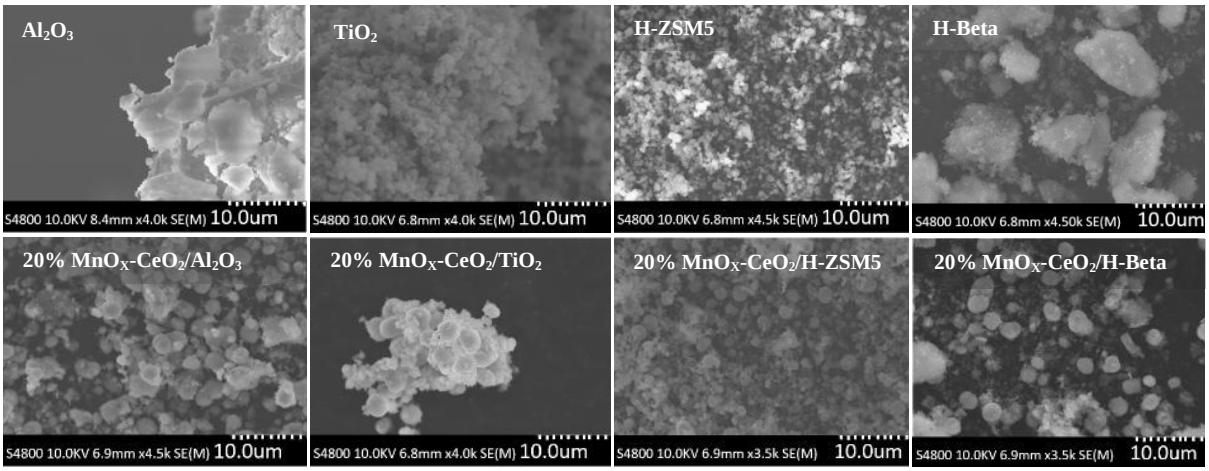

Figure 3: SEM images for the bare supports and for 20% MnO_X-CeO_2 load catalysts.

4.1.3. STEM-HAADF

In order to have a deep insight of elemental composition in the catalytic surface, the samples have been analysed by STEM-HAADF. Additionally, EDXS elemental maps were obtained for the samples.

Figure 4 and Figure 5 represent the HAADF images and the resulting maps corresponding to the 20% MnO_X-CeO_2 load supported catalysts and show certain regions in each sample to examine the spatial distribution of the active phase and the support in each catalyst. EDXS mapping for the alumina and titania supported catalysts (Figure 4) show that in the two cases the dispersion of Mn (green colour) and Ce (red colour) is good and uniform. It should be noted that in all cases even though the Ce is in lower quantities compared to Mn, it is widely dispersed and in the case of the titania Mn is present in lower quantities.

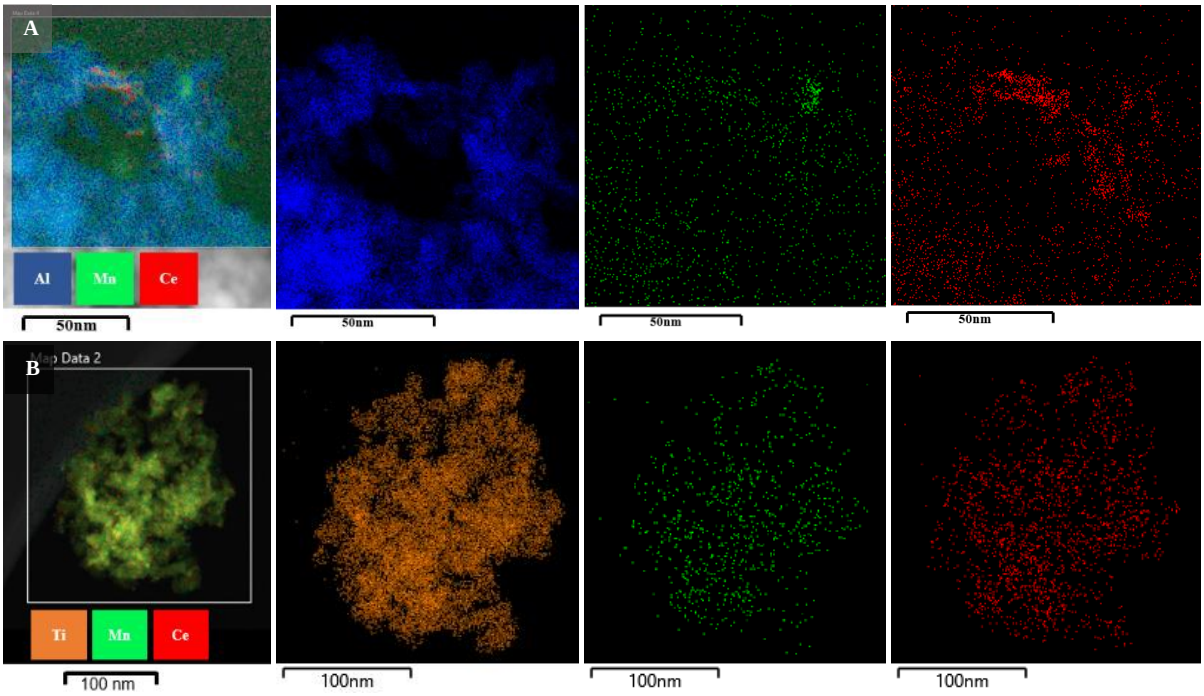

Figure 4: EDXS mapping of composition particles in the 20% MnO_X-CeO_2 load catalyst supported on: A) Al_2O_3 and B) TiO_2.

Regarding the EDXS mapping of the zeolites (Figure 5) a good interaction between the supports and the active phase is observed. While in the case of the H-Beta zeolite a uniform interaction between the active phase and the support is seen, in the case of the H-ZSM5 in some points there are agglomerations of the active phase. Nevertheless, this analysis proves the presence of the active phase together with the support in the studied catalyst and shows a good and uniform dispersion of all the elements.

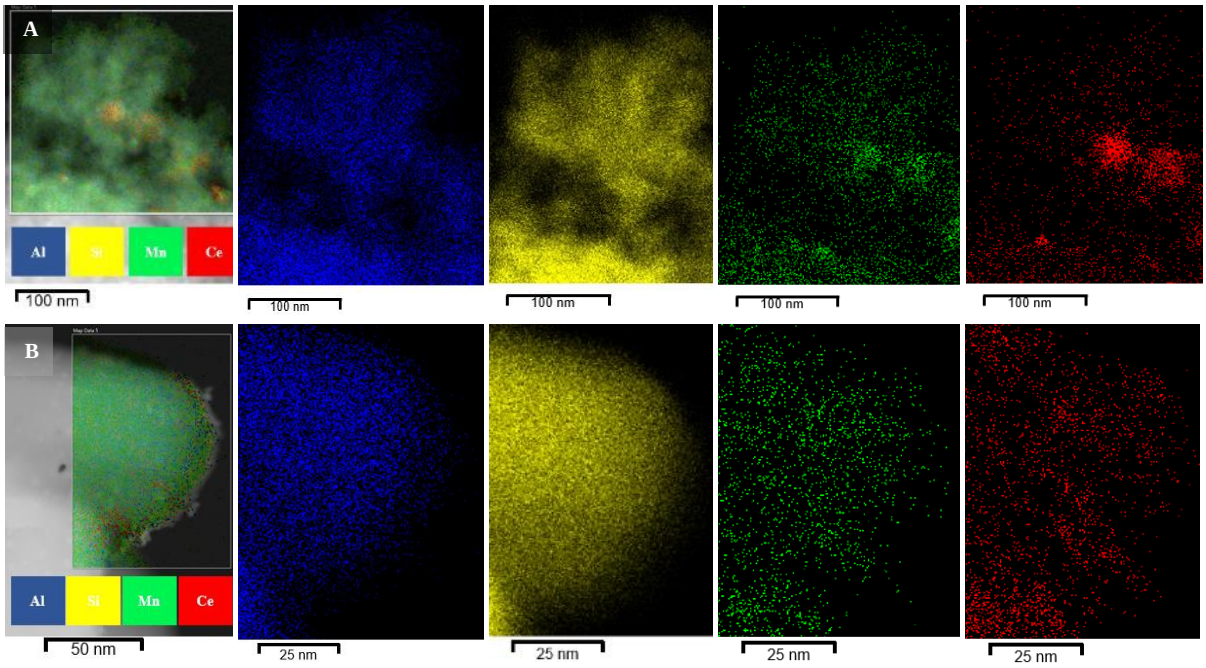

Figure 5: EDXS mapping of composition particles in the 20% MnO_X-CeO_2 load catalyst supported on: A) H-ZSM5 and B) H-Beta.

4.1.3. Physical adsorption of nitrogen

The N_2 adsorption-desorption isotherms are shown in Figure 6. The isotherms for the catalysts supported on alumina and TiO_2 show typical IV curves, according to IUPAC classification, indicating the formation of the mesoporous structure (Wang et al., 2019). In the presence of mesopores, capillary condensation will occur during adsorption and is preceded by metastable fluid state, while capillary evaporation during desorption occurs via a hemispherical meniscus, separating the vapor and the capillary condensed phase. This will result in hysteresis since pores of a specific size are filled at higher pressures and emptied at lower pressures (Groen et al., 2003). The alumina presents H1 type hysteresis loops, often associated with porous materials consisting of well-defined cylindrical-like pore channels or agglomerates of approximately uniform spheres. These spheres are evidenced by SEM images (Figure 3). Contrastingly, TiO_2 supported catalysts show H3 type hysteresis loops. Materials that give rise to H3 hysteresis have slit-shaped pores and the desorption curve of H3 hysteresis contains a slope associated with a force on the hysteresis loop, due to the so-called tensile strength effect (Alothman 2012).

On the other hand, the catalysts supported on zeolites present isotherms classified as type I, which are characteristic of microporous structures and which occurs when a large amount of gas is adsorbed at low relative pressures (Xu et al., 2018). All the samples showed the well-order structure of microporous zeolite due to similar N_2 adsorption desorption isotherms. All catalysts isotherms display a sharp rise in nitrogen uptake at low relative pressure ($P/P_0 < 0.03$), indicative of the presence of numerous micropore structures on both H-ZSM5 and H-Beta. The nitrogen uptake obviously declined after active phase introduction although this cannot be

clearly seen in Figure 6 (Zhang et al., 2019b; Wei et al., 2021). These isotherms also present an H3 type hysteresis loop. The hysteresis that occurs due to nitrogen condensation at pressures close to saturation pressures during adsorption indicates some degree of mesoporosity due to two different factors: firstly, the accumulation of MnO_X and CeO_2 nanoparticles, corroborated with SEM images; secondly, the fact that the H-ZSM5 and H-Beta support have both micro and mesopores. When the active phase is supported, as the whole support is not covered, there are still mesopores. The hysteresis is more evident in the case of the H-ZSM5 zeolite where at near 0.5 relative pressure the nitrogen desorbed volume decreases drastically.

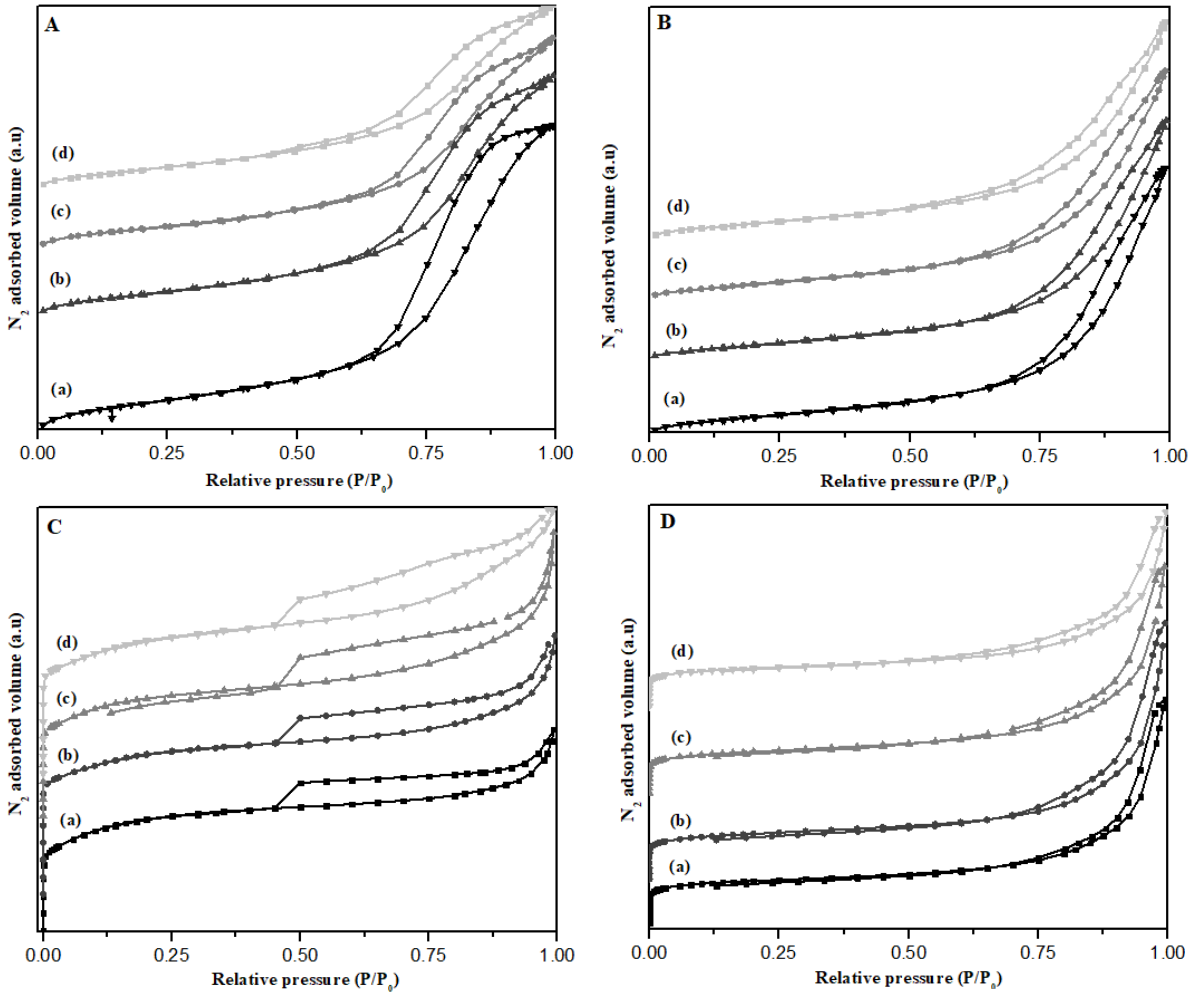

Figure 6: N_2 adsorption/desorption isotherms of the catalysts supported on: A) Al_2O_3, B) TiO_2, C) H-ZSM5 and D) H-Beta. Being a) the bare support, b) 5% MnO_X-CeO_2/support, c) 10% MnO_X-CeO_2/support and d) 20% MnO_X-CeO_2/support, respectively.

Pore size distribution plays a crucial role in SCR of NO_X reaction with ammonia (Boningari et al., 2015). Figure 7 shows the pore size distribution traces for the investigated samples. A wide distribution of pores is found for the Al_2O_3 and TiO_2 supported catalysts. In the two cases, as the active load increases, a new distribution of smaller pores appears. This distribution appears in 3.6 nm for the Al_2O_3 supported catalysts and in 3.3 nm for the TiO_2 supported catalysts. However, to see this distribution in TiO_2 supported catalysts, more active phase load is needed, only being visible in the 20% MnO_X-CeO_2/TiO_2 catalyst. Nevertheless, although pores of size close to 3 nm appear in the two cases the majority of the pores are around 70 nm, i.e., mesopores. Additionally, in the 20% MnO_X-CeO_2/TiO_2 catalyst, the unique peak seen in the lowest active phase load catalyst, divides into two different contributions. This suggests that there are two more predominant sizes than before.

In the case of the H-ZSM5 zeolite huge differences are seen comparing to the alumina and titania supported catalysts. In H-ZSM5 supported catalysts the same pore size distribution is seen in all cases attributed to microporous pores. The H-ZSM5 samples are the ones with the most uniform pore size distribution, which exhibits a predominant pore size centered at approximately 3.88 nm. Figure 7D shows that the H-Beta support presents mainly two pore sizes, centered at 8.18 and 28.73 nm. These pore sizes are maintained when the active phase is introduced, and one tiny peak appears at ca. 3.42 nm. This indicates, as observed in the N_2 adsorption/desorption isotherms (Figure 6D), the presence of both micropores and mesopores. The peak found at 3.42 nm increases as the active phase load does and moves to bigger pore sizes ending up being found at the same position as in the H-ZSM5 support. This, together with the results obtained with the rest of the supports, suggests that when the active phase is loaded, it favors a pore size between 3.3-3.9 nm.

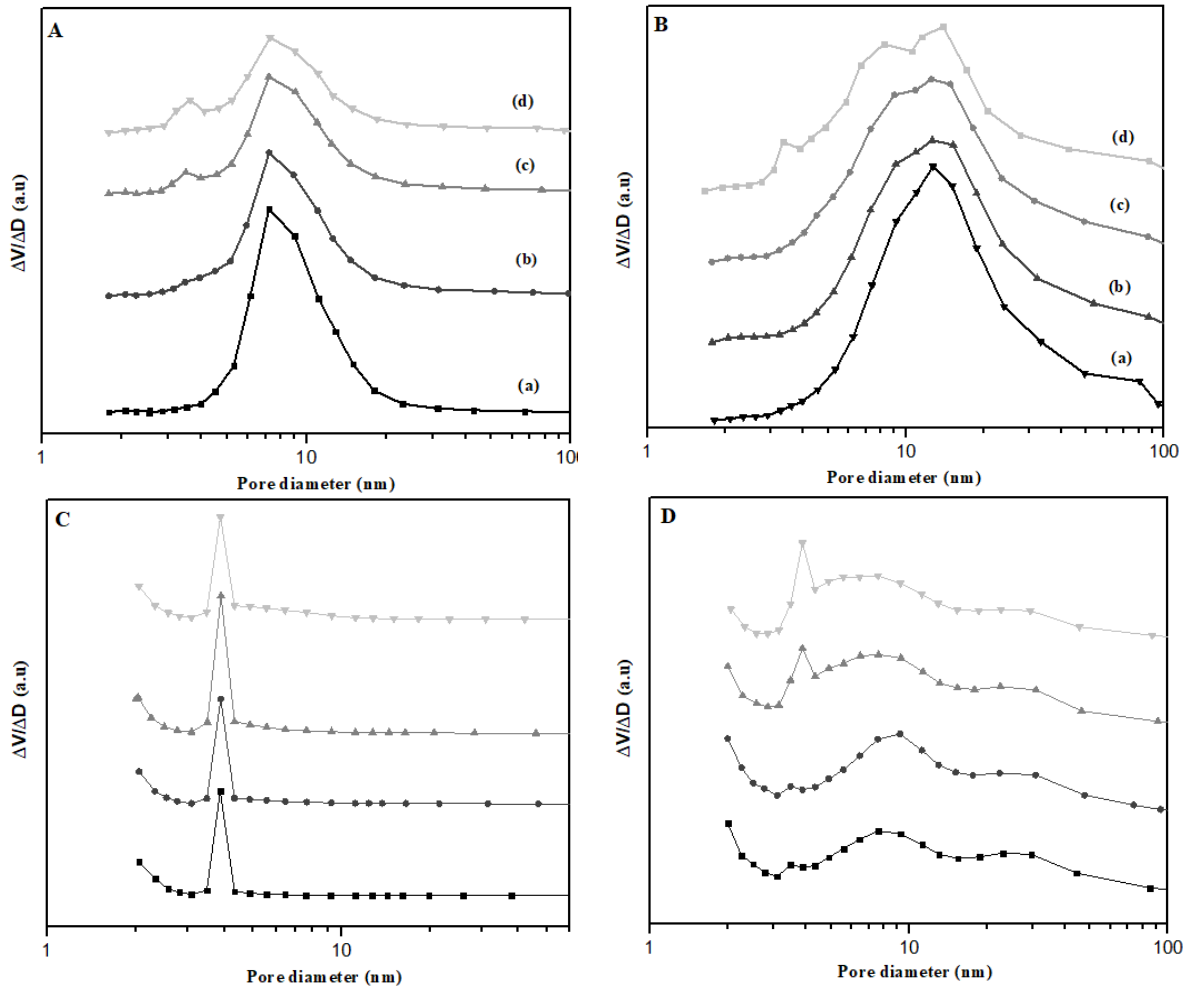

Figure 7: Pore size distribution of the catalysts supported on: A) Al_2O_3, B) TiO_2, C) H-ZSM5 and D) H-Beta. Being a) the bare support, b) 5% MnO_X-CeO_2/support, c) 10% MnO_X-CeO_2/support and d) 20% MnO_X-CeO_2/support, respectively.

BET surface area data and average pore volume are listed in Table 5. A change in the BET surface area is also reported as the active phase is increased. Comparing the different supports BET surface area remarkable differences are seen. The zeolites are the supports exhibiting the highest BET surface area. This fact gives them a good gas adsorption capacity and the possibility of obtaining a high dispersion of the active species (Quindimil-Rengel 2015). On the other hand, the titania is the support with the lowest BET surface area, which indicates that the active phase might be more agglomerated than in the other supports.

In all the samples significant changes to the textural properties are observed after the introduction of the active phase load. First, when compared to the bare supports, the BET surface area decreases considerably (10-20%), indicating that a portion of smaller pore structures on the surface are presumably covered by the bigger oxide particles. When the active phase is increased the surface area remains nearly constant and in some cases it decreases. There are two exceptions where the BET surface area increments with the active phase load: from the 10% MnO_X-CeO_2/H-ZSM5 to the 20% MnO_X-CeO_2/H-ZSM5 catalysts it raises a 6.41% and when the active phase is supported on H-Beta. This might be, in the case of the H-ZSM5, because in the 10% MnOx-CeO_2/H-ZSM5 the active phase is agglomerated in some parts of the surface, not dispersing well through all the catalyst surface. This could result in a wrong estimation of the BET surface area. The increase of the H-Beta zeolite specific surface area when the active phase is loaded, it could be because a good dispersion of the active phase (as occurs in the catalyst with lower active phase content) promotes a higher specific surface area. The good dispersion of the active phase is evidenced by STEM-HAADF images (Figure 5B).

In the case of the alumina and titania supported catalysts, the total pore volume also decreases when the active load is introduced, as well as when its content is increased. This is because a subset of pores and gaps on the support are occupied after loading the active components. In the case of the zeolites, they are formed by micropores as well as by mesopores. Practically half of the pore volume is formed by mesopores in the bare H-ZSM5 zeolite. When the active phase is loaded, this value increases, ending up being a 75% of the total pore volume. This does not mean that the total pore volume increases; in fact, the total pore volume barely varies. This is because the loss of micropores promoted by the active phase is compensated by the increase in mesoporosity. This increase in mesoporosity is mainly attributed to the low content of mesopores in the support (50%). Contrarily, the bare H-Beta zeolite is formed mainly by mesopores, which form 85% of the total pore volume. This value does not change in the 20% MnO_X-CeO_2/H-Beta catalyst (84% of the total pore volume are still mesopores). Because of the high mesoporosity in the H-Beta zeolite, the mesoporosity provided by the active phase does not have an impact. In fact, its effect is negative, negatively affecting the micropore volume, as well as the mesopore volume.

Table 5: Catalyst textural properties.

Sample	Specific surface area (m^2/g)	Change (%)	Pore volume (cm^3/g)	
			Micropore volume	Mesopore volume
Al_2O_3	225	-	-	0.618
5% MnO_X-CeO_2/Al_2O_3	178	–20.9	-	0.487
10% MnO_X-CeO_2/Al_2O_3	158	–29.9	-	0.426
20% MnO_X-CeO_2/Al_2O_3	159	–29.3	-	0.381
TiO_2	86	-	-	0.309
5% MnO_X-CeO_2/TiO_2	77	–10.5	-	0.279
10% MnO_X-CeO_2/TiO_2	77	–9.9	-	0.267
20% MnO_X-CeO_2/TiO_2	76	–11.3	-	0.255
H-ZSM5	399	-	0.116	0.114
5% MnO_X-CeO_2/H-ZSM5	319	–19.9	0.081	0.129
10% MnO_X-CeO_2/H-ZSM5	290	–27.2	0.065	0.129
20% MnO_X-CeO_2/H-ZSM5	309	–22.5	0.065	0.172
H-Beta	346	-	0.099	0.514
5% MnO_X-CeO_2/H-Beta	374	8.1	0.102	0.549
10% MnO_X-CeO_2/H-Beta	339	–2.0	0.086	0.500
20% MnO_X-CeO_2/H-Beta	312	–9.8	0.081	0.379

4.1.4. XRD Analysis

Figure 8 presents the XRD patterns obtained for the MnO_X-CeO_2 catalyst samples for each respective support. Table 6 shows the calculated crystal sizes for the observed most intense peaks. There are several differences in the XRD patterns depending on the support and the amount of active phase loaded.

Figure 8A shows the results for the catalysts supported on alumina. The support shows the most intense diffraction peaks at 46 and 67.1º (2Θ), having other less remarkable ones at 20.3, 32.7, 37.2, 39.7 and 61º (2Θ), which are associated to γ-Al_2O_3 crystalline structure (JCPDS, 050-0741) (Jiménez et al., 2015).

The load of active phase makes the diffraction peaks of the alumina become increasingly broad. This suggests a strong inhibition of the crystalline domains of the Al_2O_3 on account of the active phase metal oxides migration on the surface of the Al_2O_3. The diminution of the Al_2O_3 crystal size is an evidence of this fact (Table 6). Additional peaks appear at 28.9, 33.2, 37.4 and at 55.5º (2Θ). In the catalysts with the smallest load (5%), signals associated to α-Mn_2O_3 phase (JCPDS, 01-078-030) are seen at 33.2 and 55.5º (2Θ). The further increase in the active phase load causes a lower full width at half maximum of the α-Mn_2O_3 phase peaks and another signal appears, attributed to cerionite, characteristic of cubic fluorite structure (JCPDS, 00-004-0593) at 28.8º (2Θ). Moreover, an additional diffraction peak at 37.4º (2Θ) associated to Mn_2O_3 appears in the highest active phase load catalyst. This new diffraction peak was negligible at lower active phase contents due to the higher intensities of Al_2O_3 diffraction peaks.

It must be noticed that after increasing the active phase content, even though there is more Mn content than Ce and contrary to the expectations, the Mn_2O_3 diffraction peaks at 33.3 and at 55.5º (2Θ) nearly disappear, leading to a notably decrease of Mn_2O_3 crystal size (Table 6). This could be promoted by the interaction between the Ce and Mn, regarding that contrary to the

diminution of the Mn_2O_3 diffraction peaks, the crystallinity of CeO_2 diffraction peaks increases, as it can be seen in Table 5. In fact, in the 20% MnO_X-CeO_2 catalyst, not only does the diffraction peak of Mn_2O_3 phase at 55.5º (2Θ) loose crystallinity, but it also appears another peak associated to cerionite phase at 56.7º (2Θ). Additionally, the most intense peak of the cerionite phase is shifted towards bigger Bragg angles. This indicates that the dispersion of MnO_X on the surface of the catalyst and/or its incorporation into the CeO_2 lattice is promoted by the increasing amount of CeO_2, according to the highest amount of active phase (Yao et al., 2017; Sun et al., 2019).

Therefore, the XRD pattern of the catalysts supported on Al_2O_3 displays the presence of CeO_2, Mn_2O_3 and Al_2O_3, considered that the content of Mn and Ce is significantly smaller comparing to that of the support. A good dispersion of the active phase on the support, confirmed by STEM-HAADF images (Figure 4A), and a high interaction between the manganese and cerium is as well observed regarding the fact that when the active phase load is increased cerium peaks tend to prevail over manganese peaks.

In the case of the catalysts supported on TiO_2 (Figure 8B), the pure TiO_2 presents an intense peak at 25.5º with further peaks at 38, 48.0, 53.9, 55.1, 62.6, 68.8, 70.6 and 75.2º (2Θ) (JCPDS, 71-1169), corresponding to anatase crystal phase. No obvious diffraction peaks are observed when the active phase is supported. The factor which accounts for this phenomenon is the low supported active phase load, which is highly dispersed and exists in a poorly crystalline or amorphous state on the surface of the catalysts (Boningari et al., 2015). Nevertheless, tiny diffraction peaks of MnO_2, corresponding to pyrolusite (JCPDS, 00-050-0866) at 28.8 and 42.6º and Mn_2O_3 crystallites at 33.2º (2Θ) are discerned in the 10% and 20% MnO_X-CeO_2 catalysts. It should be noted that the peak at 28.8º (2Θ), previously associated to pyrolusite, could be also contributed by the most intense diffraction peak of CeO_2.

Furthermore, anatase crystalline size increases with active phase loading, contrary to the case of the Al_2O_3. According to N_2 physisorption results (results shown in section 4.1.3), a decrease of pore volume and surface area is observed at higher active phase loadings (Table 5). These results suggest a partial loss of the porosity of the support, caused by the active phase deposition in the TiO_2 particles. The location of this active phase elements in the TiO_2 interphase could cause a solid-state diffusion (sintering of TiO_2 crystal domain) and larger TiO_2 crystal sizes would be promoted. The same behaviour has been observed by Gallastegi-Villa et al. (2015) and Martín-Martín et al. (2021) after supporting vanadium oxide on TiO_2 anatase.

Similar XRD patterns are found in the H-ZSM5 zeolite supported catalyst (Figure 8C). The diffractogram shows peaks at 14, 14.9, 16.1, 21.1, 23.2 (the latter is its most intense peak), 23.9, 24.6, 26.8, 30.2, 45.1 and 45.7º (2Θ), which corresponds to the MFI structure of commercial ZSM-5 sample (Botas et al., 2012). The MFI phase forms the biggest crystal sizes comparing to the rest of the supports (Table 5). Even the diffraction peaks of the H-ZSM5 are maintained, when the active phase is introduced, suggesting that the loading of MnO_X and CeO_2 did not change the microstructure of the H-ZSM5 support (Wei et al., 2021), their intensities are reduced. This results in the decrease of the crystal size of the support with the increase of the active phase (Table 6).

Moreover, only in the 20% MnO_X-CeO_2/H-ZSM5 catalyst is found a weak signal arising from the CeO_2 crystallites. This suggests that the formed manganese and cerium species are in nanometre size range and/or well dispersed in the rest of the catalysts, due to their low load. The diffraction peaks corresponding to ceria are at 28.7, 33, 47.5 and 56.6º (2Θ). No diffraction peaks corresponding to MnO_X are shown, which could be due to the overlapping with

diffraction peaks of MFI structure or to the strong interaction between the Mn and Ce active metals, as it has been already proposed (Wei et al., 2021).

In addition, Figure 8D shows the diffraction patterns of the catalysts with H-Beta as support. All samples present a diffraction peak at 22.7º (2Θ) with shoulder peaks at 18.6, 21.6, 27.3 and another tiny peak at 43.9º (2Θ) which is typical for H-Beta zeolites with a BEA topological structure (Zeng et al., 2019). The active phase load and its increase clearly causes the expansion and diminution of crystallinity (evidenced by the lower crystal sizes) of BEA structure, as a consequence of surface interaction with the supported Mn and Ce oxides. Moreover, higher active phase loading also promotes the appearance of CeO_2 and MnO_2 diffraction peaks. The diffraction peaks corresponding to ceria are located at 28.9, 33, 47.5 and 56.6º (2Θ). The diffraction peak attributed to pyrolusite, on the other hand, is at 37.3º (2Θ) (Xu et al., 2018).

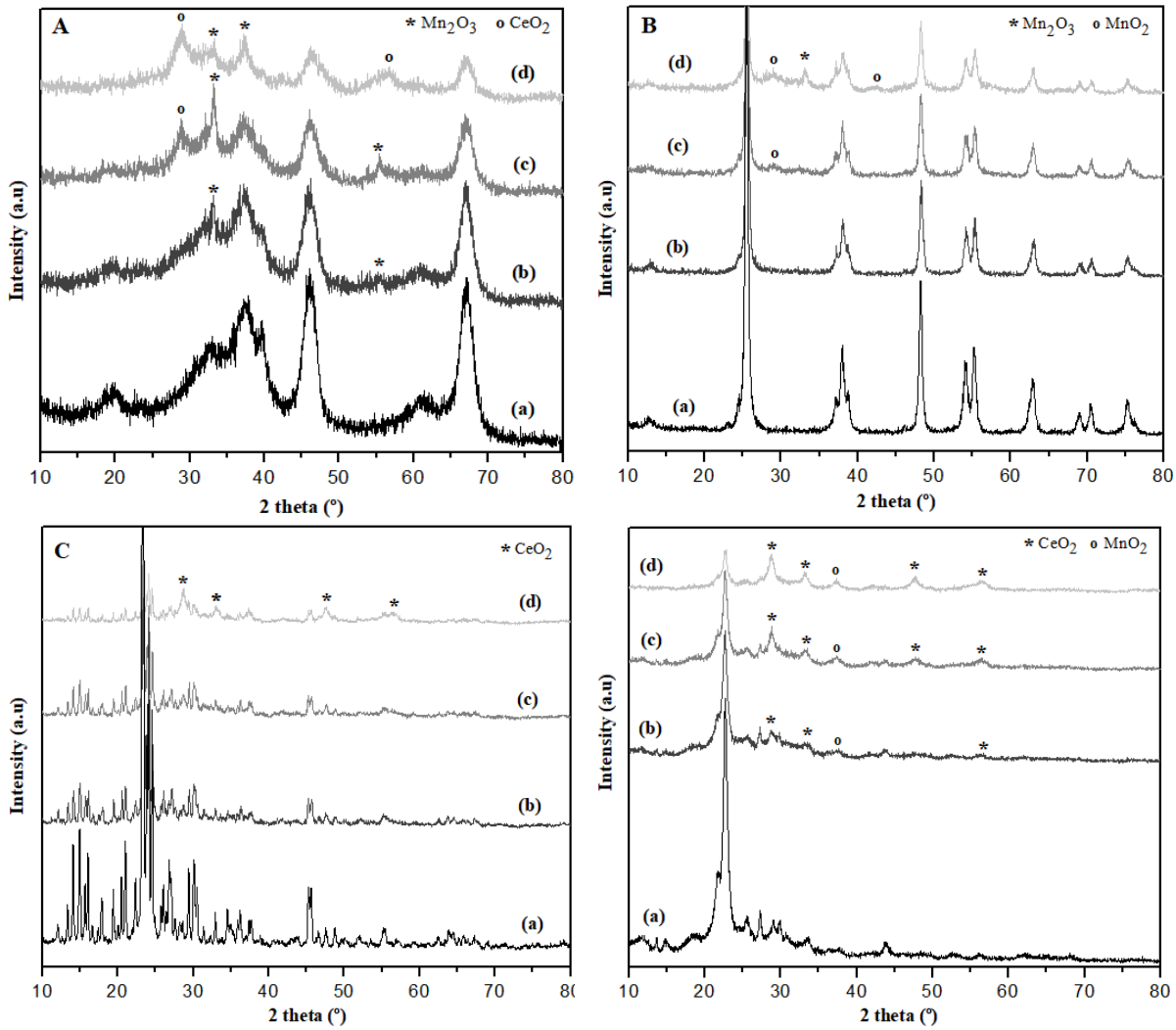

Figure 8: XRD diffractograms of the prepared catalysts supported on: A) Al_2O_3, B) TiO_2, C) H-ZSM5 and D) H-Beta. Being a) the bare support, b) 5% MnO_X-CeO_2/support, c) 10% MnO_X-CeO_2/support and d) 20% MnO_X-CeO_2/support, respectively.

Table 6: Crystal size of the supported catalysts.

Sample	Phase	Position (2Θ) (º)	Crystal size (nm)
Al_2O_3	γ-Al_2O_3	67.1	4
10% MnO_X-CeO_2/Al_2O_3	CeO_2	28.9	2
10% MnO_X-CeO_2/Al_2O_3	Mn_2O_3	33.2	8
20% MnO_X-CeO_2/Al_2O_3	Al_2O_3	67.1	4
20% MnO_X-CeO_2/Al_2O_3	CeO_2	28.9	3
20% MnO_X-CeO_2/Al_2O_3	Mn_2O_3	33.2	3
TiO_2	TiO_2	25.5	19
20% MnO_X-CeO_2/TiO_2	TiO_2	25.5	20
H-ZSM5	MFI	23.2	33
20% MnO_X-CeO_2/H-ZSM5	MFI	23.2	31
20% MnO_X-CeO_2/H-ZSM5	CeO_2	28.7	8
H-Beta	BEA	22.7	11
20% MnO_X-CeO_2/H-Beta	BEA	22.7	8
20% MnO_X-CeO_2/H-Beta	CeO_2	28.9	6
20% MnO_X-CeO_2/H-Beta	MnO_2	37.3	5

4.1.5. NH_3-Temperature Programmed Desorption

The acidity of the catalysts has a significant influence in the low-temperature NH_3-SCR and oxidation reaction performance (Liu et al., 2020). Therefore, the acid site distribution of the prepared catalysts has been investigated via NH_3-TPD. In this technique, the desorption temperature is taken as a qualitative measure of the strength of the acidity, linking the desorption peaks at low temperatures (≤170 ºC) to weak acid sites whereas the ones at high temperatures are related to strong acid sites (>170 ºC). The amount of the acid sites is related to the integrated area of the peaks. Quantitative results for acidity, calculated by time-integration of the TCD signal, are summarized in Table 7.

Regarding total acidity, active phase deposition does not have a clear positive effect on the catalysts with Al_2O_3 and TiO_2 supports. On the contrary, total acidity is improved after Mn and Ce deposition in the zeolite-based catalysts, independently of the active phase content. In the case of the alumina, the acidity does not improve when the active phase is loaded. Actually, the total acidity decreases in the catalyst with the lowest active phase load, which is when the active phase is more dispersed. The further increase of active phase content makes the total acidity to increase. However, these values compared to the one obtained with the bare support hardly change. This could be due to the fact that when the active phase is loaded on the support, the surface area decreases, making less NH_3 to adsorb, causing the total acidity to decrease in comparison to the support. This is confirmed by the results of the total acidity per unit area. While the total acidity with the active phase load per gram decreases, per square meter increases.

Regarding the strong/weak total acidity ratio, the dispersion of the active phase has a negative effect on the strong acidity. Interestingly, the tendency of the calculated ratios coincides with the respective tendency of the total acidity, with the exception of the 20% MnO_X-CeO_2/Al_2O_3, in which the strong/weak acidity ratio is slightly higher and total acidity decreases.

Calculated per unit area the TiO_2 support has the highest total acidity of all samples. This high acidity of the TiO_2 is said to be beneficial for the abatement reactions by different authors

(Zhang et al., 2019a). The TiO_2 support is the only case in which the maximum total acidity is found in the bare support. This fact could be associated to the excellent acid properties of TiO_2, which would be negatively affected by the active phase deposition. Nevertheless, with the increase of the active phase the total acidity as well as the strong/weak acidity ratio are incremented. This means that the total acidity is highly influenced by the strong/weak ratio. It has to be pointed out that the titania supported catalysts are the only ones that when incremented the active phase load up to 20% MnO_X-CeO_2 a good dispersion of the active phase is still seen, being the only one in which no negative effects are seen with this active phase load. This can be confirmed by STEM-HAADF images (Figure 4B), where a good dispersion of the active phase over the titania support is observed.

Regarding to zeolites, total acidity is notably higher than in the other supports, ca. it doubles the total acidity of the titania and the alumina. In fact, zeolites have been chosen as supports based on their acidic properties. The larger acidity values of zeolites are probably associated to their higher BET surface area, since after expressing the acidity per unit area, this value strongly decays in comparison to the other supports.

In the zeolite-based catalysts the increase in the active phase up to the 10% MnO_X-CeO_2/zeolite catalyst leads to higher total acidities; however, the further increase has a detrimental effect, just like in the case of the alumina supported catalysts. It should be noted, however, that contrary to what has been observed in the case of the alumina, the total acidity increases in the catalyst with the lowest active phase load. This could be associated to the high surface area of the zeolites (results shown in section 4.1.3) in comparison to alumina.

The calculated ratios are coincident with the respective tendency of the total acidity, as in the prior cases. This means, as previously mentioned, that the strong/weak ratio has an important influence in the total acidity. The increase of the strong/weak acidity indicates that strong acid sites are favoured with the load of active phase. This indicates, in the case of the zeolites, that the active phase promotes a stronger acidity. Oppositely to the case of the alumina, in the case of the zeolites low active phase content promotes a good interaction between the support and the active phase, so the high interaction between support and active phase seems to favour strong acidity. However, when the active phase is incremented, an agglomeration is promoted, decreasing the interaction with the support and active phase. Consequently, it has a negative effect on the total acidity. That is why regarding to the acidity and in the case of the zeolites, the optimum load is 10% MnO_X-CeO_2.

Figure 9A-D shows the NH_3 desorption profiles of the samples supported on Al_2O_3, TiO_2, H-ZSM5 and BETA, respectively. Regarding to the NH_3 desorption profiles of the bare supports, they are as follows:

A) Al_2O_3 shows a major desorption peak around 95 ºC and a shoulder at higher temperatures (ca. 220 ºC). The former is associated to weak acid sites while the latter is linked to strong acid sites.

B) TiO_2 presents a main desorption peak around 106 ºC followed by a progressive decrease of NH_3 desorption at higher temperatures, suggesting mainly two types of acid sites in the surface of the sample, which are weak and strong acid sites.

C) The bare H-ZSM5 zeolite exhibits two different desorption peaks. The first one at 100 ºC with a shoulder at 170 ºC, attributed to NH_3 chemisorbed on weaker acid sites and the other peak is found at around 350 ºC showing the presence of strong acid sites.

D) In the case of Beta zeolite, two signals at high and low temperature can be distinguished. It shows a principal desorption peak around 125 ºC and a secondary tiny peak around 330 ºC, demonstrating the presence of weak and strong acid sites.

When the active phase is introduced, its presence leads to different NH_3 desorption profiles depending on the support. Although similar features are observed after increasing it. Two different NH_3 desorption peaks are distinguished. One at low temperatures (100-120 ºC) attributed to weak acid sites and another one at high temperatures attributed to strong acid sites, the position of the latter differs depending on the support. In the case of the alumina and the titania, this last peak is found at 266 ºC and in the case of the zeolites at 311 ºC.

In all cases, the desorption peak of the support at the lowest temperature is maintained when the active phase is introduced and increased. However, its intensity decreases, comparing each support with the highest active phase catalyst. This means a decrease in the total weak acidity and indicates that even though weak acid sites are still present in the sample, their number decreases. This can as well be seen comparing the calculated total weak/strong acidity ratio (Table 7).

Regarding to strong acidity, in the case of the Al_2O_3 supported catalysts the second peak at high temperatures appears when the active phase is introduced. This peak moves towards lower temperatures when the active phase load is increased. This also happens at the highest temperature desorption peak of the catalysts supported on TiO_2 and H-ZSM5 zeolite. This means that the strength of the acid sites is weakened as the active phase is increased.

Contrastingly, the second desorption peak in the H-Beta zeolite supported catalysts moves slightly towards higher temperatures when the active phase is increased and a shoulder appears around 420 ºC, having the strongest acid sites comparing with the rest of the catalysts. It should be noticed that strong acid sites are reduced in the highest active phase load catalysts supported on zeolites. In the case of the H-ZSM5-based catalysts the observed signal decreases dramatically after the peak found at 31 ºC, while in the H-Beta based catalysts the second peak linked to strong acidity decreases, as it can be seen in Figure 9C and 9D. This also can have influence making the 10% MnO_X-CeO_2/zeolite have a higher total acidity and a higher strong/weak acidity ratio.

On the other hand, the quantitative results previously analyzed for the titania are better understood with the NH_3 desorption profiles. In the case of the titania support there is a unique wide desorption peak, meaning that a wide variety of different strength acid sites exists. With the active phase this wide desorption peak divides into two narrower desorption peaks. The area of these two desorption peaks is smaller than the one of the support. That is why the total acidity is higher in the support, even when calculated per unit area. The strong/weak acidity ratio is smaller in the higher active phase load catalyst. This is because even in the support the area below the strong acid sites range is bigger; in the range of weak acid sites is as well bigger. In the 20% MnO_X-CeO_2/TiO_2 catalyst the strong acid sites are favoured from the weak acid sites; that is why the calculated ratio between them is bigger.

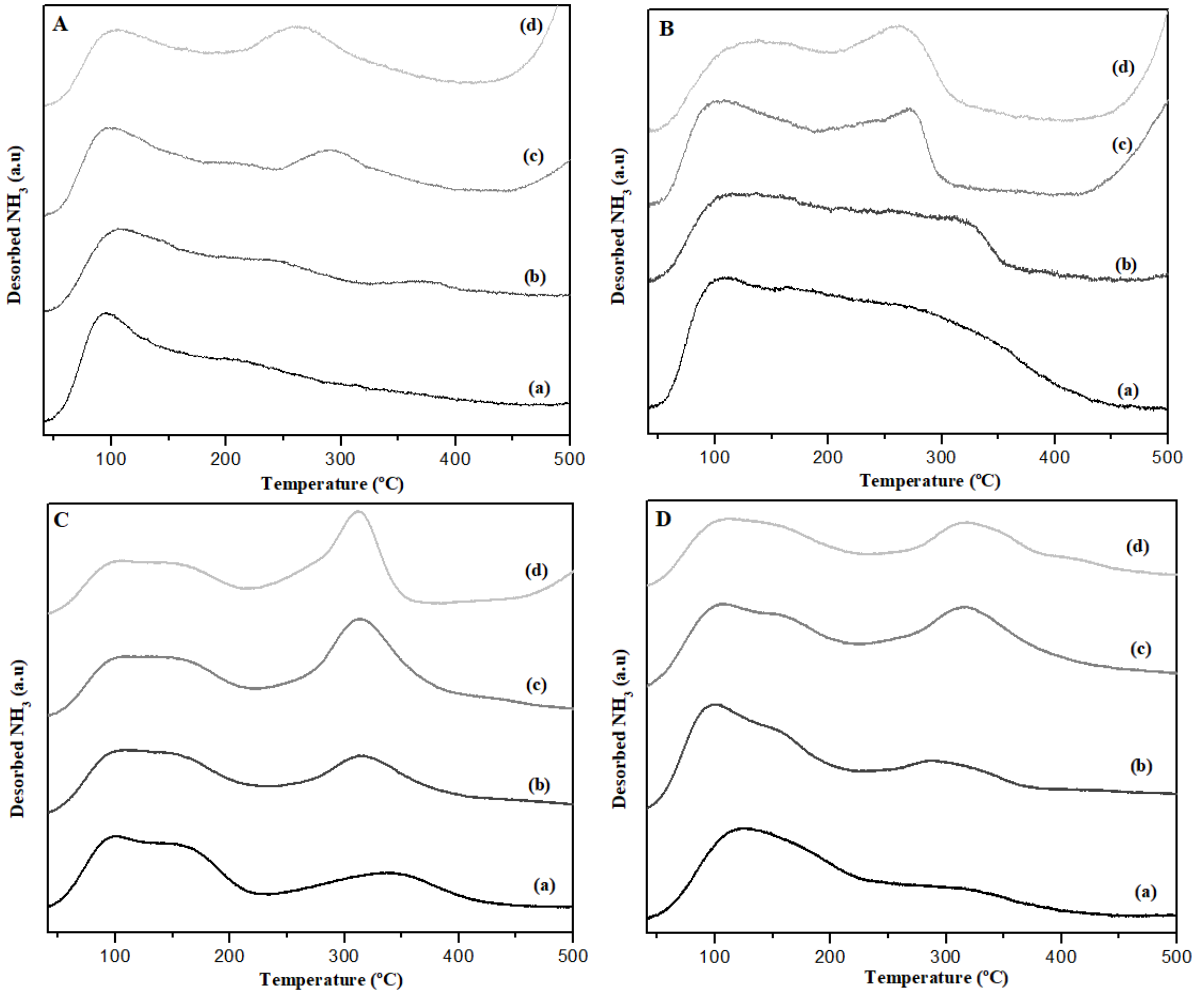

Figure 9: NH_3-TPD profiles of the prepared catalysts supported on: A) Al_2O_3, B) TiO_2, C) H-ZSM5 and D) H-Beta. Being a) the bare support, b) 5% MnO_X-CeO_2/support, c) 10% MnO_X-CeO_2/support and d) 20% MnO_X-CeO_2/support, respectively.

Table 7: Acid properties of the supported catalysts.

Sample	NH_3 (µmol/g)	NH_3 (µmol/m^2)	Strong/Weak
Al_2O_3	236	1.05	1.7
5% MnO_X-CeO_2/Al_2O_3	200	1.13	1.3
10% MnO_X-CeO_2/Al_2O_3	240	1.57	1.6
20% MnO_X-CeO_2/Al_2O_3	233	1.47	1.9
TiO_2	242	2.82	1.6
5% MnO_X-CeO_2/TiO_2	148	1.92	1.5
10% MnO_X-CeO_2/TiO_2	154	1.98	1.2
20% MnO_X-CeO_2/TiO_2	170	2.23	1.7
H-ZSM5	419	1.05	0.8
5% MnO_X-CeO_2/H-ZSM5	490	1.68	1.4
10% MnO_X-CeO_2/H-ZSM5	573	1.97	2.0
20% MnO_X-CeO_2/H-ZSM5	497	1.61	1.8
H-Beta	483	1.39	0.9
5% MnO_X-CeO_2/H-Beta	582	1.56	1.0
10% MnO_X-CeO_2/H-Beta	657	1.94	1.7
20% MnO_X-CeO_2/H-Beta	539	1.72	1.6

As mentioned prior in the materials and methods section (section 3.2.5), NH_3 could react with the surface oxygen of the catalyst forming nitrogen oxides. These nitrogen oxides would affect the NH_3 desorption profiles. The TCD works comparing the heat loss rate between a reference gas and the outlet stream, so the created nitrogen oxides could interfere. In order to check this issue, a mass spectrometer was used. NO and N_2O were the only nitrogen oxygen detected through their corresponding m/z=30 and m/z=44, respectively. Results are displayed in Figure 10.

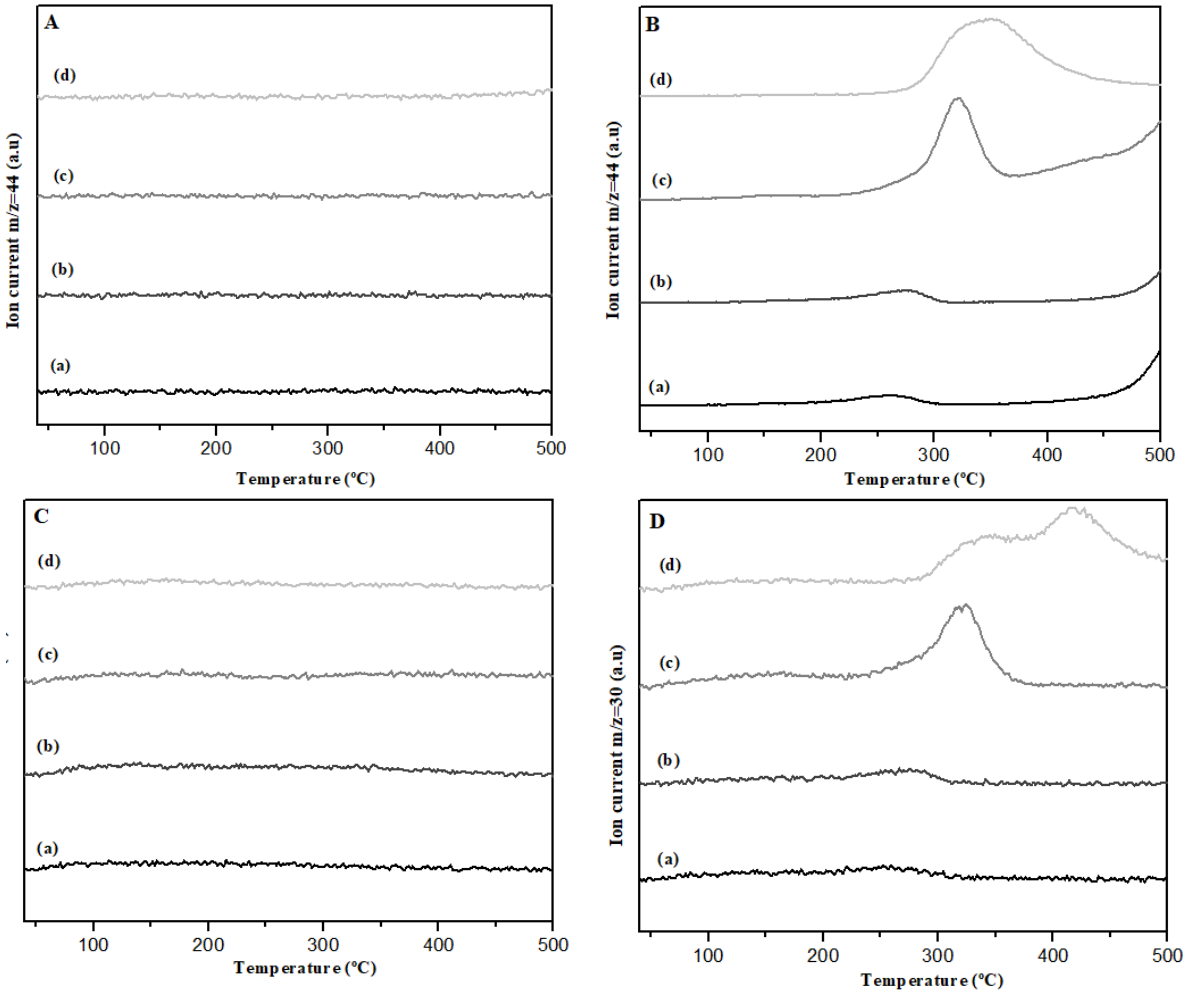

Figure 10: Signals arising from the mass spectrometer for the bare supports (A and C) and for the 20% MnO_X-CeO_2/support catalysts (B and D), being: a) Al_2O_3, b) TiO_2, c) H-SZM_5 and d) H-Beta. For N_2O (A and B) and NO (C and D) masses.

The first notable fact is that nitrogen oxides are only formed when the active phase is supported, as no signal attributed to these masses is observed in the case of the supports. This means that the formed nitrogen oxides correspond to the incorporation of the active phase. This is because the active phase has a high oxidizing character.

Nevertheless, in the case of NO, it is also slightly formed in the supports themselves, observed in Figure 10C, as the signals do not form exactly straight lines. This implies that a small part of the oxygen present in the structure of the support reacts with the NH_3 forming NO. The same form is observed in the 20% MnO_X-CeO_2/support catalysts with the addition of the signal corresponding to the active phase.

In the case of the Al_2O_3 a small peak corresponding to N_2O is observed at 264 ºC and at 260 ºC for NO. Regarding TiO_2, similar peaks to the ones of the alumina are seen but in this case at ca. 280 ºC. In addition, the H-ZSM5 and H-Beta zeolites show a unique peak of N_2O at 344 ºC and at 321 ºC, respectively. Nevertheless, a clear difference exists in the case of the signal attributed to NO. A wider peak is observed at 416 ºC with a shoulder at 336 ºC for the H-ZSM5 and in the case of H-Beta at 325 ºC with a shoulder at 318 ºC.

A main conclusion is obtained: in all the catalysts nitrogen oxides are formed in the same temperature range, which is at high temperatures, corresponding to strong acidity. Thus, the desorption of nitrogen oxides in the NH_3 desorption profiles is corroborated and suggests that ammonia is oxidised on the catalyst surface when it is adsorbed mainly on strong acidic centres.

4.1.6. H_2-Temperature Programmed Reduction

The oxidation and reduction performances over the MnO_X-CeO_2 active phase supported on Al_2O_3, TiO_2, H-ZSM5 and H-Beta zeolites directly related to their catalytic properties and have a key effect on the SCR and oxidation reactions (Zhang et al., 2019a). Hence, to analyse these properties hydrogen temperature-programmed reduction was accomplished. Obtained H_2 consumption curves are shown in Figure 11.

In this figure, it can be observed that none of the supports, with the exception of TiO_2, presents reduction peaks. This is because the hydrogen consumption of the supports is negligible comparing to the one occurring when the active phase load is introduced, with the exception of the titania. Thus, when the active phase is supported the resulting reduction peaks correspond to this load. H_2-TPR profiles can be divided in two parts:

I) The first is the one in which all the catalysts exhibit two broad reduction peaks, in the range of 100-550 °C, which are attributed to stepwise reduction of MnO_X overlapped with the reduction of surface CeO_2 to Ce_2O_3. Several works in the literature agree that MnO_2 reduction in catalysts is practically indistinguishable from that of Mn_2O_3. Therefore, many authors associate H_2 consumption at low temperature (around 300 °C) to the reduction of MnO_2/Mn_2O_3 to Mn_3O_4, and H_2 consumption at intermediate temperature (around 400 °C) to the reduction of Mn_3O_4 to MnO and surface CeO_2 when explaining TPR profiles (Shen et al., 2017).

II) The second, which consists of the reduction of bulk ceria, CeO_2 to Ce_2O_3, is found at higher temperatures, above 600 ºC. Even this consumption is not observed in Figure 11 due to the small load of cerium and the way the data have been represented (Yao et al., 2017; Tang et al., 2021).

In all the cases, the peaks are seen in the first low temperature range. Comparing with the bare active phase reduction profile, which in literature is reported to show two strongly overlapped peaks at 266 and 300 °C and other additional peak at 400 °C (Martín-Martín et al., 2020), with the use of a support the reduction peaks appear at lower temperatures. This indicates a good dispersion of the active phase. A good dispersion of the active phase favours a good interaction with the support, which favours a lower temperature reduction. This can be evidenced by STEM-HAADF images (Figure 4-5), where a good dispersion of the active phase and interaction with the support is seen in all the supported catalysts.

H_2 consumption profiles of the alumina supported catalyst are the most distinct ones. When the active phase is loaded two different H_2 consumptions can be observed, in the range of 100-

500 ºC, associated to the reduction of manganese oxides and surface ceria. When the active phase is increased, two main differences are observed: firstly, the peak found at high temperatures increases considerably; secondly, the contribution found at the middle gains intensity and becomes wider, which makes the most intense peak drift to higher temperatures, from 375 to 400 ºC. In the same way, the peak found at the lowest temperature is moved to lower temperatures, from 230 to 214 ºC. The middle peak seems to divide in two different contributions in the highest active phase load catalyst. This could be linked to the existing different Mn species in high oxidation state which are the ones reduced at this temperature range, which can be confirmed by literature (Martín-Martín et al., 2020). This different Mn species could be, on the one hand, the Mn which has high interaction with the support and with the Ce. On the other hand, it could be the reduction of Mn in crystalline form. The latter could be corroborated with the XRD results, where it is seen that in the 20% MnO_X-CeO_2/Al_2O_3 catalyst ceria phase is favoured. This all indicates that electronic interactions existed between MnO_X, CeO_2 and the support for these samples.

Regarding to bare titania, as it has been previously mentioned, it is the only case in which a clear H_2 consumption is monitored. This reduction peak is located at 563 ºC with a tiny shoulder at 581 ºC, which is ascribed to the reduction of the surface Ti^{4+} ions (Bratan et al., 2017). When the active phase is loaded, this peak moves towards lower temperatures (459 ºC) and when the active phase content increases it disappears. The Mn-Ce metal oxides supported on TiO_2 samples mainly exhibit two asymmetrical reduction peaks. The first one has a shoulder. This shoulder could suggest the reduction of different high oxidation state Mn species or different high oxidation state Mn species interacting in different ways, just like explained on the TPR profiles of the alumina supported catalysts. This peak moves towards lower temperatures as the active phase increases. This low-temperature shift of the reduction peak can be attributed to the formation of more surface oxygen vacancies, as a consequence of active phase and support interaction, which will facilitate the enhanced oxygen mobility or activate reactants in SCR reaction (Boningari et al., 2015). On the other hand, the area below the two peaks increases remarkably with the active phase load; this is because, obviously, samples with higher active contents have a larger H_2 consumption.

The zeolites present similar H_2-TPR profiles, with the exception of the shoulder present in the first peak of H-Beta supported catalysts, which diminishes with the active phase load. The two bare zeolites are lacking of redox abilities (Wei et al., 2021). When the active phase is supported two different reduction peaks are observed in the two cases, in the same temperature range associated to the consecutive reduction steps of MnO_X. Their intensity increases with the active phase load, just like in the case of alumina and titania supported catalysts. In the 20% MnO_X-CeO_2/zeolite catalyst, the first peak is observed at 280 ºC. The second one is found at a temperature range of 390-395 ºC and it is wider than the first one.

It should be noticed that, in the case of the H-ZSM5 support, it is the only one in which its XRD pattern does not display the presence of manganese oxides; however, the reduction peaks shown in Figure 11C, are associated to manganese oxides. This suggests that even manganese is in a highly dispersed state and, in a higher degree of interaction, it has a great influence in redox properties. This is very interesting, because it explains why it is the only catalyst with a unique contribution in the first reduction peak. In the catalysts supported on alumina, titania and H-Beta zeolite, shoulders appear in this first reduction peak, as Figure 11 shows. In their XRD patterns there are peaks associated to crystalline manganese oxides. Therefore, there could be Mn interacting with the support and Ce, and Mn interacting with only Mn (crystalline Mn aggregates). This would create different contributions in the first reduction peak. This confirms the hypothesis suggested for the titania and the alumina.

Table 8 shows the quantification of the H_2 consumed in each reduction profile of Figure 11. It is clear that TPR shows that the active phase load allows to improve the reducibility of the samples. In all cases the H_2 consumption increases with the active phase load. The worst redox properties correspond to bare zeolites, confirming their lack of redox abilities. However, when the active phase is supported, the redox properties are improved, even more than in the catalysts supported on alumina. The titania supported catalysts, on the other hand, are the ones with the best redox properties. This is because the electronic interactions between the titania and the active phase favor the reducibility of this catalysts.

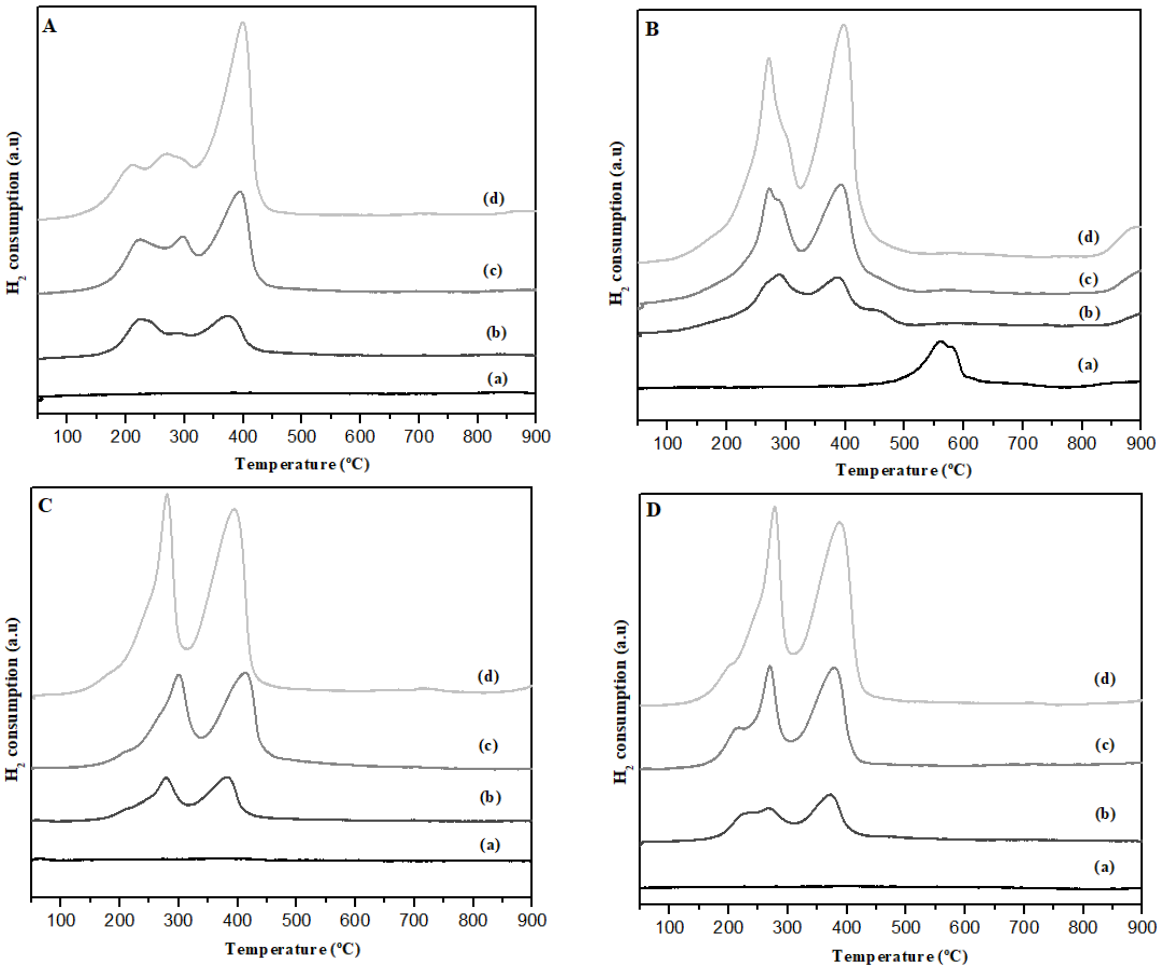

Figure 11: H_2-TPR profiles of the prepared catalysts supported on: A) Al_2O_3, B) TiO_2, C) H-ZSM5 and D) H-Beta. Being a) the bare support, b) 5% MnO_X-CeO_2/support, c) 10% MnO_X-CeO_2/support and d) 20% MnO_X-CeO_2/support, respectively.

Table 8: Acid properties of the supported catalysts.

Sample	H_2 consumption (mmol H_2/g)	Sample	H_2 consumption (mmol H_2/g)
Al_2O_3	0.48	TiO_2	0.44
5% MnO_X-CeO_2/Al_2O_3	1.07	5% MnO_X-CeO_2/TiO_2	1.33
10% MnO_X-CeO_2/Al_2O_3	1.62	10% MnO_X-CeO_2/TiO_2	1.78
20% MnO_X-CeO_2/Al_2O_3	2.38	20% MnO_X-CeO_2/TiO_2	2.94
H-ZSM5	0.23	H-Beta	0.19
5% MnO_X-CeO_2/H-ZSM5	0.75	5% MnO_X-CeO_2/H-Beta	0.96
10% MnO_X-CeO_2/H-ZSM5	1.45	10% MnO_X-CeO_2/H-Beta	1.43
20% MnO_X-CeO_2/H-ZSM5	2.62	20% MnO_X-CeO_2/H-Beta	2.52

As a resume of the characterization section, SEM and STEM-HAADF techniques have corroborated the good dispersion of the active phase over the different supports. The good dispersion of the active phase greatly impacts in the physico-chemical properties of the catalysts. In the case of morphological characteristic, the deposition of the active phase causes a decrease in the specific surface area and pore volume of the samples due to the blocking of the porous structure of the supports. The latter does not occur in the H-ZSM5 supported catalysts, in which the pore volume increases with active phase loading. This is because after depositing the active phase, the samples gain a certain degree of mesoporosity, whose contribution to the total pore volume is greater than the volume of micropores lost.

The high dispersion of the active phase has been also corroborated by XRD by means of the no appearance of Ce and Mn oxide diffractions peaks in the catalysts with the lowest active phase loading (with few exceptions). The increase in the active phase loading promotes both Ce and Mn oxide diffraction peaks, which indicate the presence of surface agglomerates of active phase. Regarding these diffraction peaks, it should be noted that fluorite phase, characteristic of pure CeO_2 and cerium oxide interacting with Mn, appears in all families of supported catalysts, especially in those with the highest Mn loading. Manganese oxide diffraction peaks appear as well, although associated to different species, thus, alumina and titania supported catalysts promote Mn_2O_3 phase and H-Beta supported catalysts MnO_2. The nature of the support also affects to the interaction between the metals that compose the active phase, in this sense, alumina is the support that promotes the higher interaction between Mn and Ce, evidenced by the shifts of the most intense peak of fluorite phase. This feature is a key factor for low temperature SCR and oxidation reactions.

The presence of different Mn species in high oxidation state, as consequence of the presence of Mn in different environments (Mn oxide, Mn interacting with the support and Mn interacting with Ce) has been corroborated by H_2-TPR, through the different contributions that compose the first reduction peak of Mn. In addition, H_2-TPR has evidenced an improvement of redox properties after supporting the active phase, due to the shift of the H_2 consumption profile to lower temperatures. Supporting the active phase not only improves the redox properties, but it also improves the acid properties. In this sense, total acidity becomes larger with the increase of the active phase loading. This improvement of total acidity is associated to the increase of strong acidity contribution.

4.2. CATALYTIC ACTIVITY

4.2.1. Assessment of the supported alternative catalysts for the simultaneous abatement of NO_X and PCDD/Fs.

Characteristic curves, referred to as ignition or light-off curves, have been obtained as shown in Figure 13 and Figure 14, for NO reduction and o-DCB oxidation, respectively.

Figure 13 shows the NO conversions. Bare supports present different characteristic curves. The bare alumina hardly affects the abatement of NO. Nonetheless, the titania and zeolites exhibit similar profiles, achieving high conversions at high temperatures. There are three remarkable facts. In the case of the H-ZSM5 the conversion rises up to 94.4% at 425 ºC, temperature at which NO conversion over bare H-ZSM5 is higher than over MnO_X- CeO_2/H- ZSM5; this also happens at high temperatures (> 400 ºC) in the case of the titania. In the case of the H-Beta zeolite, it is the only support that maintains nearly constant the conversion of NO at high temperatures. These good results of the zeolites and the titania could be associated to their acidity (section 4.1.5) and, in the case of the zeolites, to their surface properties as well (section

4.1.3). H-Beta zeolite has BEA topological structure as XRD results have shown (section 4.1.4). This structure and the structure of the H-ZSM5 zeolite have a 3-dimensional pore structure that ensures better diffusion of the reaction molecules allowing better interaction with the active sites (Younes et al., 2021). Specifically, the better high-temperature performance of H-Beta may be associated with its high mesoporosity.

The last remarkable fact regarding the ignition curves of the supports is that at low temperatures (< 200 ºC) NO conversions are negative; in the case of the alumina it also happens at high temperatures. This is because a higher concentration of NO is exiting the reactor compared to the one that enters. This could be because the support favours side-reactions which create NO. Probably they are favouring the oxidation of ammonia.

The active phase load significantly improves the catalytic activity in the low temperature region and similar light-off curves are observed. They can be divided in three different zones: in the first one, from 75 to 125 ºC, NO conversion increases with temperature; in the second one, from 125 to 250 ºC, the conversion remains constant above 95%, and in the third one the decay of the conversion is seen when the temperature increases. All catalysts show outstanding low temperature NH_3-SCR activity.

Figure 12 shows the light-off curve of unsupported mixed oxide 85Mn-15Ce sample, which allows better analysis of the effect of active phase supporting. The differences are outstanding. Firstly, in the low temperature region, NO conversion is near 100% and secondly, high activity is maintained through the wide range of 75-250 ºC (Martín-Martín et al., 2020).

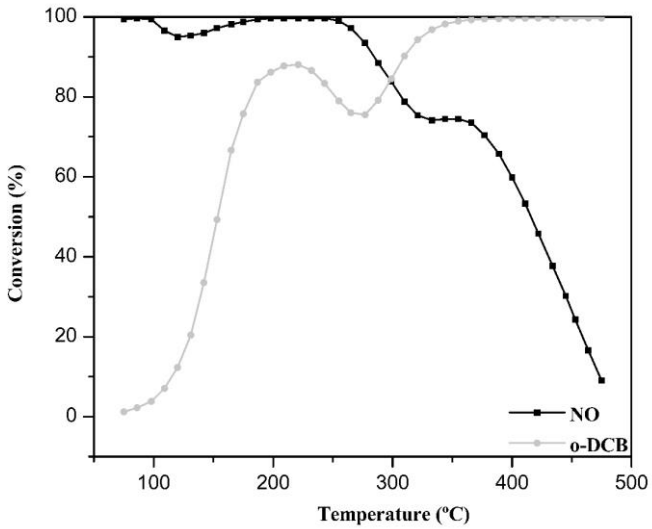

Figure 12: Ignition curves of NO and o-DCB in simultaneous abatement over 85Mn-15Ce.

The first difference then, is that the supported catalysts are not sufficiently active to start the reaction with high conversions; that is why the low temperature zone appears. This can be confirmed with the increase of the active phase: the catalyst improves its catalytic activity in the low temperature zone and higher NO conversions are observed. This fact, which is observed in the catalysts supported on the four different supports, is most notable in the case of alumina, where a conversion of ca. 95% is reached at the lowest temperatures. This better catalytic behaviour at low temperatures in the alumina supported catalysts may be related to the higher interaction between Ce and Mn observed in XRD. In fact, XRD showed evidence of a decrease in Mn crystallinity at higher active phase loadings, due to the promotion of the interaction with Ce. Because the upper temperature limits of the high-activity temperature windows of all

samples are very similar (where the medium temperature zone ends), the shift in the lower temperature limits effectively widened the high-activity temperature window as the active phase content increases (Wang et al., 2019). This high-activity temperature window is wider in the 20% MnO_X-CeO_2 active phase load catalysts and in the case of the ones supported on alumina and on titania the high-activity temperature window is very similar to the bare active phase catalyst. In the case of the zeolites, this temperature window is shifted to higher temperatures, which will be later on discussed.

NO conversion decays at temperatures above 250 ºC because of the appearance of side reactions, these side reactions do not only consume the reactants involved in the SCR reaction, but they also form more NO. The most important side reaction taking place is known to be the NH_3 oxidation (Yao et al., 2017), as concluded in previous research work. They also conclude that the small plateau found at high temperatures is due to the o-DCB effect (Martín-Martín et al., 2021b).

Despite the positive effect of the active phase at low temperatures, at high temperatures it has the opposite effect. This is because the active phase has a high oxidative power, favouring the oxidation, what is beneficial at low temperatures but has a fatal effect at high temperatures, since it promotes the oxidation of ammonia. The increase of the oxidising properties with increasing active phase content has already been evidenced with NH_3-TPD technique (section 4.2.5), through the increase of the strong acidity, which was found to be responsible for the oxidation of the adsorbed NH_3, due to the stronger interactions between the catalyst and the reactant.

It can be concluded that the zeolites inhibit the decay of the conversion of NO at high temperatures. This inhibition is associated to the use of this type of supports and is more noticeable on H-Beta supported catalysts. This fact allows to widen the operational window of high conversions at high temperatures. In fact, the range of NO conversions greater than 90% is 105-320 ºC for 20% MnO_X-CeO_2/H-ZSM5 and 105-380 ºC for 20% MnO_X-CeO_2/H-Beta, while for the bare active phase is 75-250 ºC.

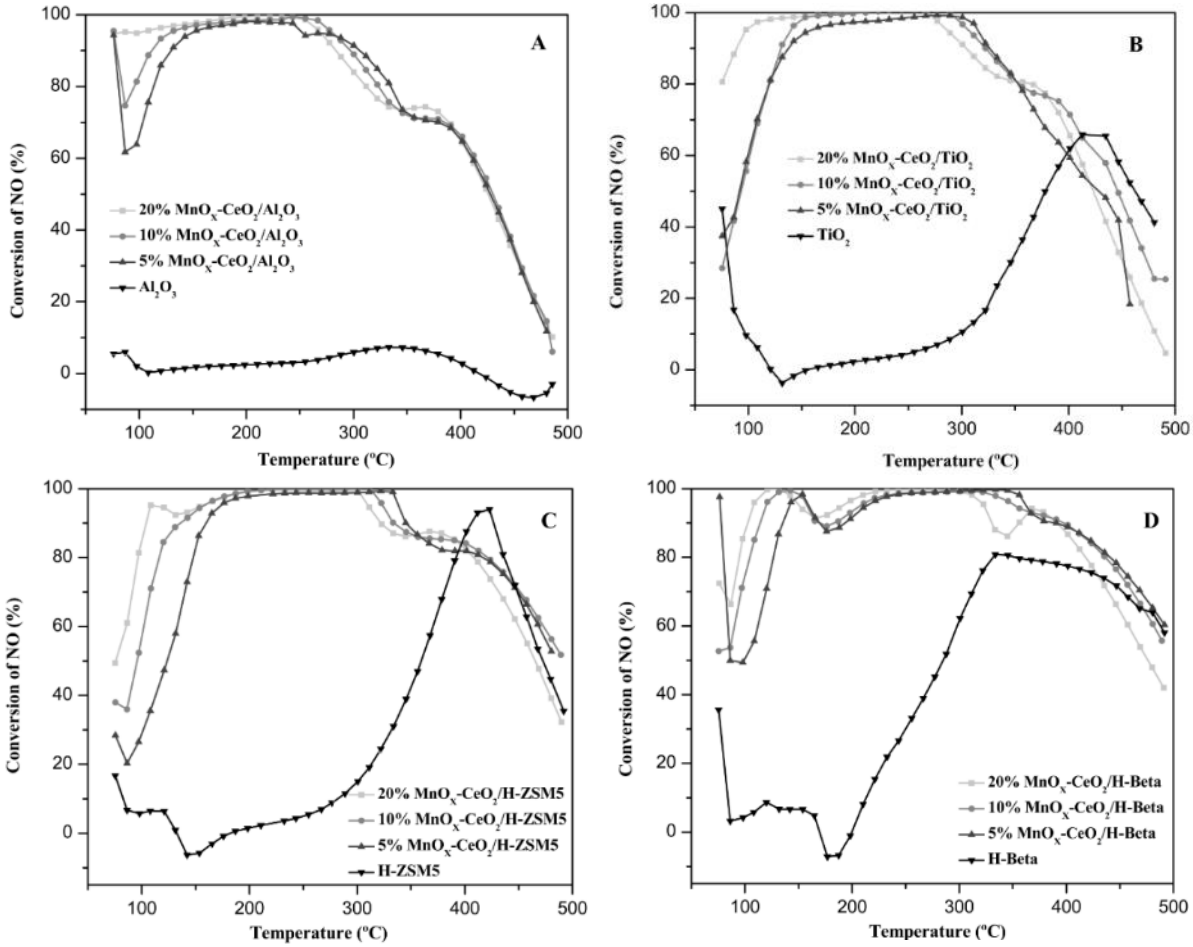

Figure 13: Ignition curves of NO over catalysts supported on: A) Al_2O_3, B) TiO_2, C) H-ZSM5 and D) H-Beta.

On the other hand, Figure 14 shows the o-DCB conversion results. NO reduction occurs at lower temperature than o-DCB oxidation; however, the two reactions present high conversions at the same temperature range, indicating that the simultaneous abatement of NO_X and PCDD/Fs is feasible in MSW treatment plants, just like concluded in previous research of the TQSA group.

The activity of the bare supports differs significantly among them. The alumina, as in the case of the SCR reaction, is not active for o-DCB oxidation. In the case of the titania, it can be seen that conversion increases significantly above 350 ºC. Similarly, o-DCB conversion over H- ZSM5 is low below 425 ºC, and it significantly increases above this temperature. H-Beta is the best bare support since conversion increases significantly above 275 ºC. These good results could be because of its high surface area, composed mainly of mesopores, and its acid properties.

When the active phase is supported a similar light-off curve shape is observed: firstly, the conversion rises up to 250 ºC. From this temperature on, the conversion drops and then rises anew until full conversion is reached. However, depending on the support and the active phase load, they differentiate in the achieved maximum conversion and the temperature at which this maximum and total conversion are reached.

Independently to the support, the increase of active phase makes the ignition curve to shift to lower temperatures. For example, total conversion is reached 35, 75, 25 and 30 ºC below when

using the 20% MnO_X-CeO_2 active phase load catalyst than when using their corresponding 5% MnO_X-CeO_2 one, in catalysts supported on alumina, titania, H-ZSM5 and H-Beta, respectively. In addition, comparing the maximum found at lower temperatures of the 5% MnO_X-CeO_2 active phase catalyst with the one obtained in the 20% MnO_X-CeO_2 catalyst, the one achieved in the highest active phase load catalyst is higher, especially, in the case of the catalysts supported on titania and on zeolites; e.g., in the maximum of the 5% MnO_X-CeO_2/TiO_2 catalyst the o-DCB conversion is 47% while in the 20% MnO_X-CeO_2/TiO_2 catalyst is 72%.

The best results are observed in the highest active phase load due to the higher oxidising power conferred by the active phase, as evidenced by the higher strong acidity as the load increases in the NH_3-TPD (section 4.1.5). Additionally, the catalysts supported on titania and alumina present a better conversion in the o-DCB maximum at lower temperatures than the zeolites. This peak at lower temperatures is associated to the good oxidising properties due to the high interaction between manganese and cerium, which generates oxygen vacancies (Martín-Martín et al., 2020). The fact that alumina and titania have less surface area means that manganese and cerium can interact more strongly and, hence, they present better oxidising properties at low temperatures.

Figure 12 shows that the o-DCB ignition curve of the 85Mn-15Ce presents a maximum where a conversion of 90% is reached whereas total o-DCB conversion is reached at 325 ºC. Hence, the activity of supported MnO_X-CeO_2 is not improved with respect to bare MnO_X-CeO_2.

The characteristic rise and drop of o-DCB conversion in the medium temperature range is noteworthy. This drop could be associated to a competition between the oxidation reaction and the parallel reactions of the SCR reaction that produce the drop in NO conversion, as these occur in the same temperature range. In previous work of the research group, different experiments were done. One of them, the analysis of o-DCB oxidation in the absence of SCR gases. This experiment showed the presence of this same fluctuation, suggesting that the fluctuation is not due to mentioned competition (Martín-Martín et al., 2021b). Wang et al. observed the same fluctuation in the oxidation of o-DCB on MnO_X-CeO_2 (Wang et al., 2008), so the combination of both results suggests that this could be intrinsic to the oxidation of chlorobenzenes over MnO_X-CeO_2 formulations. However, these authors do not propose the reason of it. In this research work, it is proposed that this fluctuation of the conversion of o-DCB could be associated to a change in the oxidation reaction mechanism, which will be discussed below.

At high temperatures o-DCB conversion rises again. This is because at high temperatures the oxidation is favoured. In the bare active phase total conversion is reached at 325 ºC. In the case of the supported catalysts with the highest active phase load total conversion is reached at 375 ºC in all the cases, with the exception of H-Beta, that total conversion is reached at 333 ºC, widening the optimum temperature range, and obtaining a similar result to the one obtained with the bare active phase.

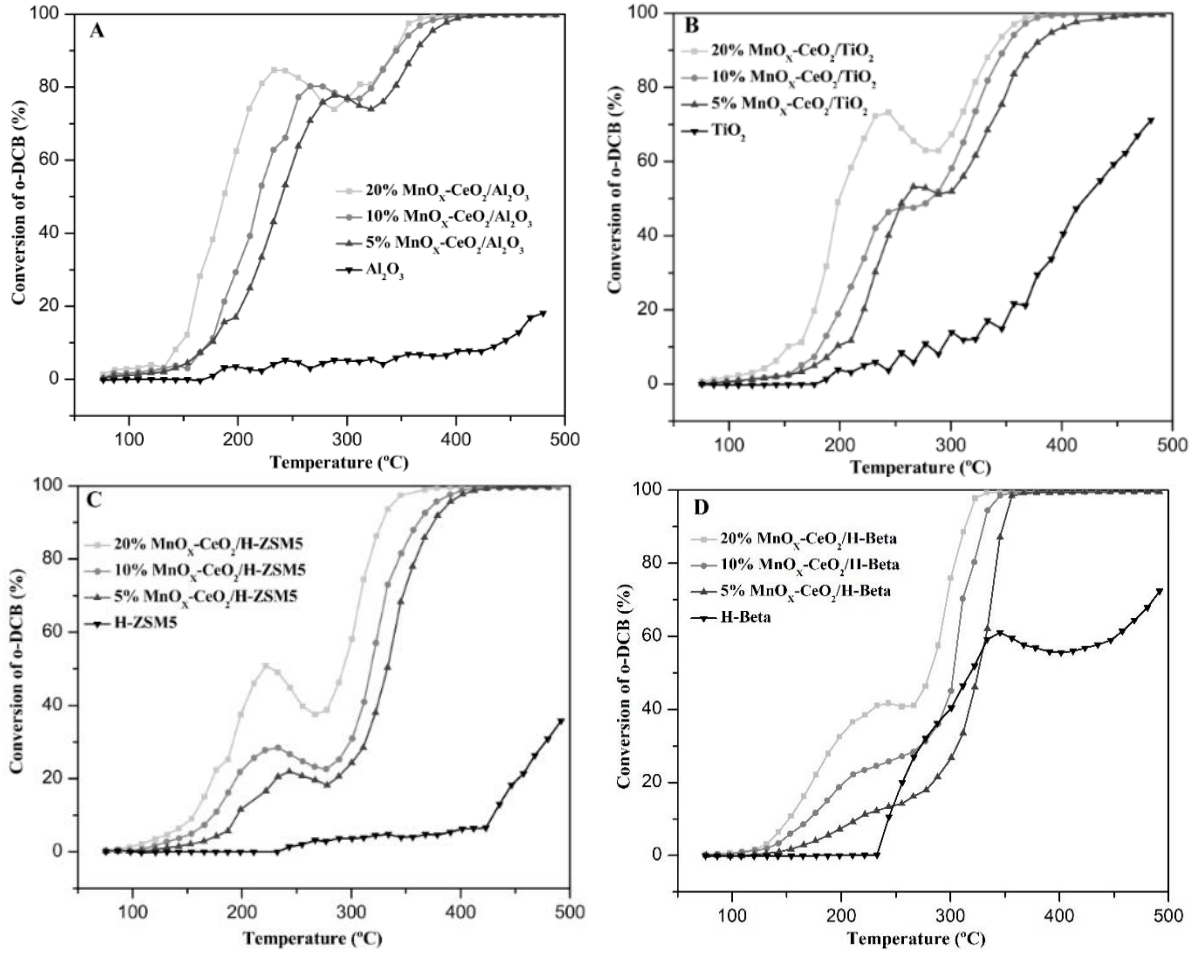

Figure 14: Ignition curves of o-DCB over catalysts supported on: A) Al_2O_3, B) TiO_2, C) H-ZSM5 and D) H-Beta.

4.2.2. Analysis of side-reactions

In the previous section, it has been concluded that the results are negatively affected by side-reactions. Specifically, the SCR reaction is clearly affected at high temperatures. Side-reactions are the reactions taking place in parallel to the two main abatement reactions, which lead to the creation of by-products. Hence, in this section, as an attempt to analyse the side-reactions taking place and understand better the obtained catalytic results, the generated by-products are analysed.

In SCR, N_2O and NO_2 are found to be the main by-products. On the one hand, N_2O can be formed in the ammonia oxidation or in the non-selective SCR reaction. Figure 15 shows that the bare supports do not form N_2O, except for a small amount above 400 ºC. Therefore, N_2O is formed due to the active phase. The formation of N_2O increases with the temperature reaching its maximum at approximately 215 ºC. Nevertheless, in all the supported catalysts, this maximum is smaller than in the case of the bare 85Mn-15Ce catalyst, as in the latter the maximum N_2O concentration is 160 ppm (Martín-Martín et al., 2020). All the N_2O formation profiles are similar at low and high temperatures, with the exception of the TiO_2 at high temperatures. With the active phase a second maximum appears at higher temperatures (400 ºC). In the case of the titania, this second peak is visible in all the supported catalysts and appears at slightly higher temperatures.

The fact that N_2O profiles are composed by two maxima may be associated to the two chemical reactions forming it, NH_3 oxidation and the non-selective reduction of NO. According to literature, the contribution of each reaction would depend on the temperature: non-selective SCR takes place at the whole temperature range, while NH_3 oxidation is the origin of N_2O formation at high temperatures (Martín-Martín et al., 2020; Ibarbia, 2017).

Another difference seen when the active phase increases, is that even the maximum concentration is nearly the same, the N_2O profiles shift to lower temperatures. Some authors consider that the formation of N_2O is related to well-ordered MnO_X crystalline phase due to the presence of highly reactive oxygen (Tae et al., 2001; Kang et al., 2006) This could be the case, confirmed by the XRD results (section 4.1.4) which show the presence of MnO_X crystallites with the increase of active phase content. Besides, with the active phase load, the oxidative power increases, which also helps to shift the formation of N_2O to lower temperatures.

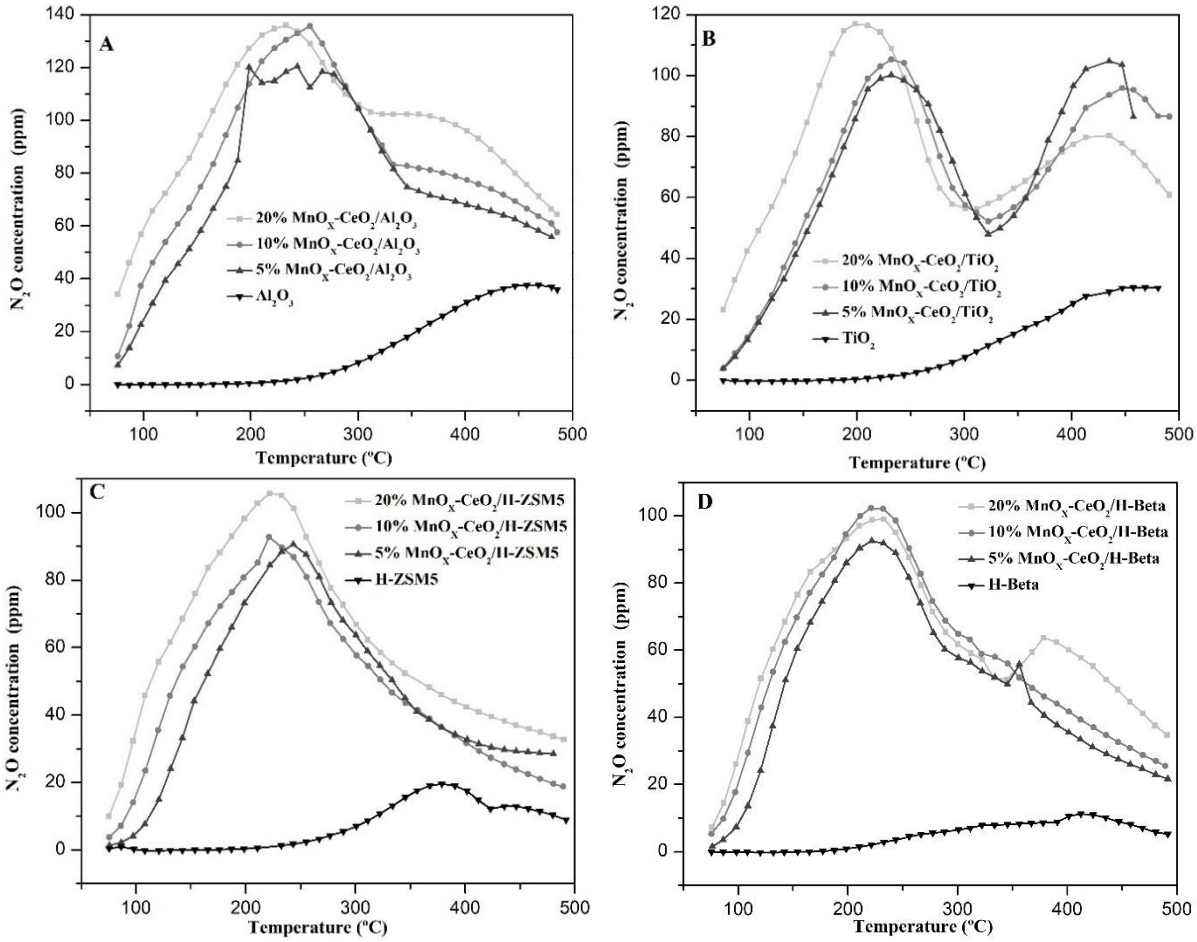

Figure 15: N_2O concentration evolution of catalysts supported on: A) Al_2O_3, B) TiO_2, C) H-ZSM5 and D) H-Beta.

Regarding the concentration profiles of NO_2, results are presented in Figure 16. The oxidation of NO and the NH_3 oxidation are related with the formation of NO_2 and in literature both of them were confirmed to be responsible for the formation of NO_2 at high temperatures (Martín-Martín et al., 2021a).

Just like in the prior case the NO_2 is formed by the load of active phase on the support. It is only formed at high temperatures and just like in the case of the formation of N_2O, the NO_2 concentration profiles move towards lower temperatures when the active phase is supported.

This is understandable, because as the active phase increases the oxidative power increases, due to better oxygen mobility (Martín-Martín et al., 2020).

Hence, the formation of these two by-products at high temperatures (Figure 15 and 16) corroborates the occurrence of side-reactions which make the conversion of NO to diminish. However, comparing the formation of the SCR reaction by-products of the supported catalysts with those of bare MnO_X-CeO_2, it is observed that supporting the active phase improves the selectivity of the SCR reaction, as in all the cases less by-products are formed (Martín-Martín et al., 2020).

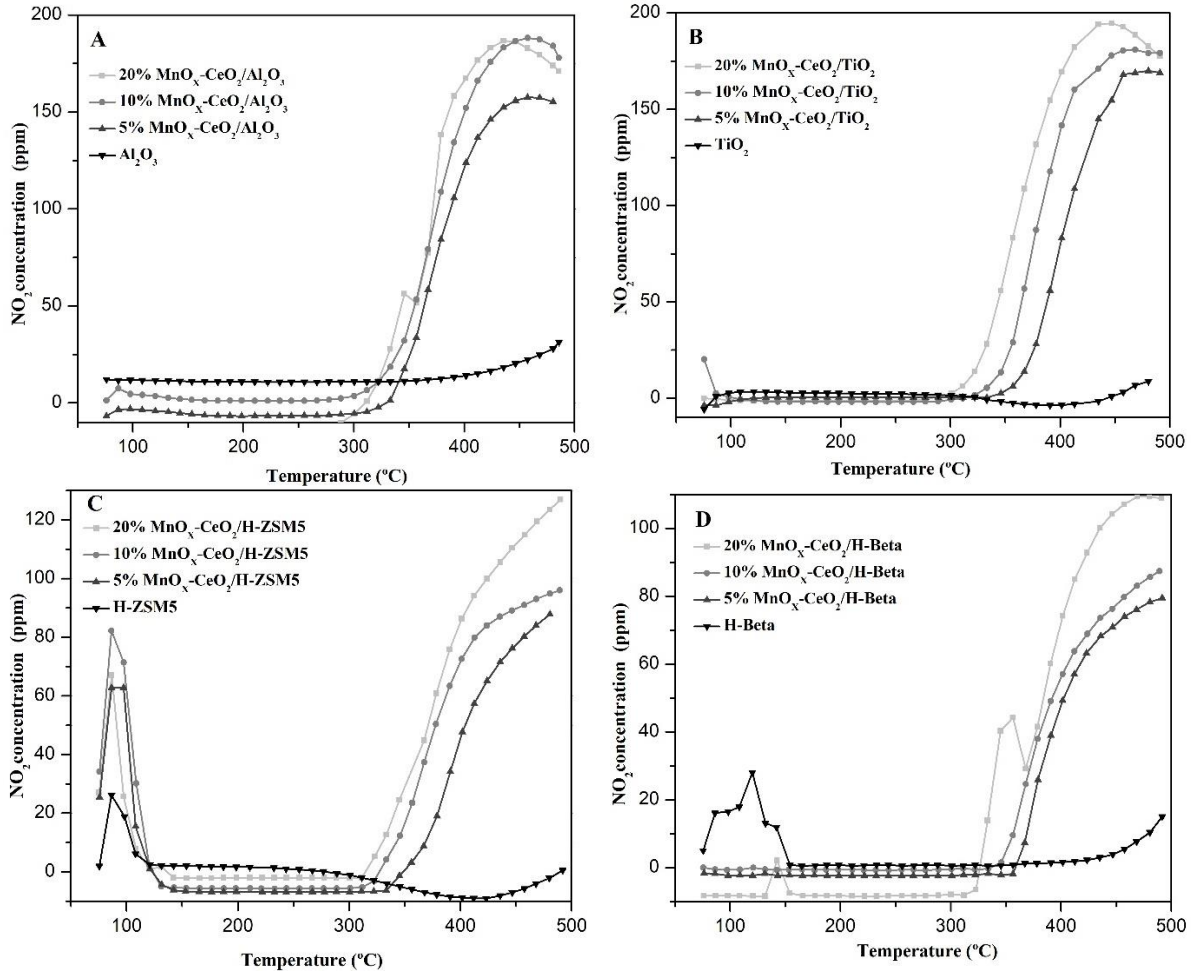

Figure 16: NO_2 concentration evolution of catalysts supported on: A) Al_2O_3, B) TiO_2, C) H-ZSM5 and D) H-Beta.

The main by-product of the o-DCB oxidation reaction is CO. CO concentration profiles are presented in Figure 17. The formation of CO is seen at the bare supports in the case of the titania and zeolites at high temperatures. However, the active phase is the main precursor of this reaction by-product. The increase of the active phase load, as in the previous cases, makes the concentration profile of CO to move to lower temperatures, due to the increasing oxidative power. Nevertheless, contrarily to the previous cases, the produced CO is slightly smaller with the active phase content.

When the active phase is loaded, CO is formed approximately at 350 ºC. This confirms what has been previously said to explain the diminution of o-DCB conversion in the medium temperature range, as it can be seen in Figure 14. It has been suggested that the reaction changes

its reaction pathway at this temperature range. This change in the reaction pathway makes total oxidation not to be reached, creating CO. Thus, Figure 17 is another evidence of the change in the reaction pathway. At higher temperatures CO concentration diminishes because the reaction between the surface oxygen of the catalyst and the reagent is more easily promoted, completing the total oxidation, and generating CO_2 instead of CO. Then oxygen vacancies of the surface of the catalyst are regenerated with the surrounding oxygen. This reaction synthesis method is known as the Mars-Van Krevelen mechanism.

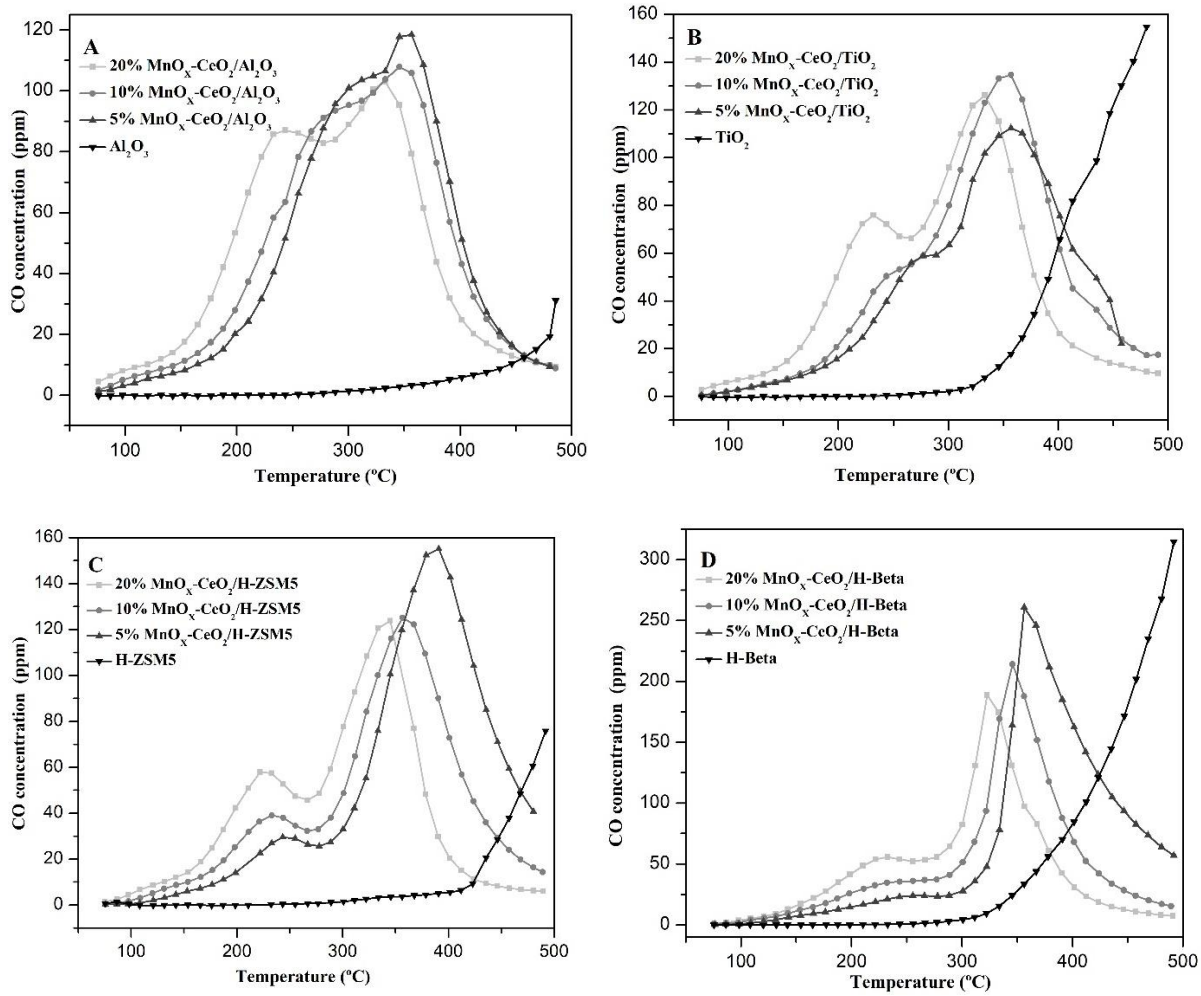

Figure 17: CO concentration evolution of catalysts supported on: A) Al_2O_3, B) TiO_2, C) H-ZSM5 and D) H-Beta.

Although carbon monoxide is the main by-product of the o-DCB oxidation reaction, other chlorinated organic by-products could be formed. Prior studies revealed that the active phase forms tetrachloroethylene and trichlorobenzene in the temperature range of 275-420 ºC (Martín-Martín et al., 2020). However, when it is loaded, no chlorinated organic by-products are formed in the case of the catalysts supported on alumina and titania; so, a promotion towards total oxidation is promoted by these supports.

Nonetheless, Figure 18 shows the formation of trichlorobenzene in the case of the catalysts supported on zeolites. As it is seen, it is formed in the range of 300 to 400 ºC in the case of the H- ZSM5 supported catalysts and in the range of 250 to 350 ºC in the case of H- Beta supported catalysts. This, together with the results obtained of the conversion of o-DCB and the peak in the CO production suggest that under such conditions there is a change in the reaction

mechanism, favouring oxidation via a route involving a greater number of intermediate by-products. This is because the temperature at which the formation of trichlorobenzene is seen coincides with the rise of the conversion of o-DCB after its drop. In the two cases, the trichlorobenzene formation moves towards lower temperatures when the active phase load increases, due to the higher oxidative power. Apart from trichlorobenzene no other chlorinated organic by-product has been formed, while in the active phase also tetrachloroethylene is formed. Thus, it can be concluded that in this area better results are obtained with the use of a support.

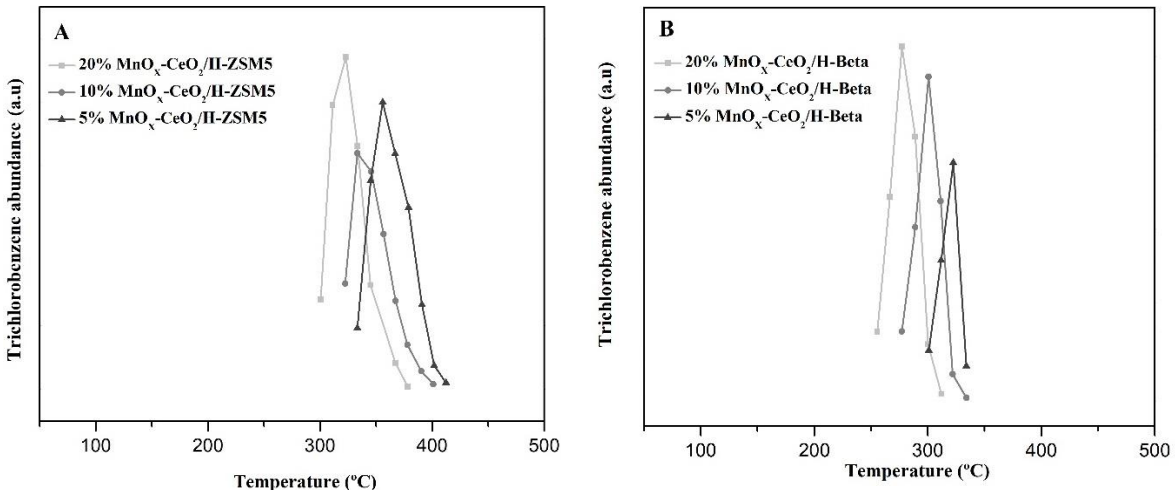

Figure 18: Trichlorobenzene produced in o-DCB oxidation reaction by zeolite supported catalysts: A) H-ZSM5 and B) H-Beta.

4.2.3. Stability tests

There is a key aspect in reactions involving catalytic oxidation of VOCs which has not been mentioned heretofore: time-deactivation. Deactivation is an actual problem in the simultaneous abatement of NO_X and PCDD/Fs and is caused by the deposition of detrimental species over the active sites that promote the reactions (Liu et al., 2013). For this reason, the 20% MnO_X-CeO_2 load supported catalysts were tested during 24 hours in the simultaneous NH_3-SCR and o-DCB oxidation at two different temperatures (200 and 300 ºC), in order to study the two regions where an increase of o-DCB conversion takes place, and at the same time, the NO_X conversions are the best. The stability tests were done only to the different 20% MnO_X-CeO_2 load supported catalysts because they were the ones showing the best NO and o-DCB conversion results. Results are shown in Figure 19.

SCR results show that NO conversion increases initially and after one hour, it stabilizes at 97% in all catalysts at 200 ºC. On the other hand, at this temperature, the o-DCB conversion shows a decrease, so a clear deactivation of these catalysts occurs for oxidation reaction. In fact, after 4-5 hours all the catalysts show no conversion of o-DCB. The fact that the SCR reaction keeps conversion constant and the o-DCB conversion declines indicates that the reactions occur at different sites at these conditions; since if both were happening at the same active sites, as the active centre is deactivated, the conversion of NO would have also decreased.

In the case of the stability test at 300 ºC, better results are obtained. Although the conversions of the SCR reaction are smaller, being 86, 87, 93 and 88% for the alumina, titania, H-ZSM5 and H-Beta catalyst, they are constant throughout the experiment, with the exception of the first hour, where the conversions slightly decay. On the other hand, the conversions of o-DCB are notably higher comparing to those obtained at 200 ºC, especially in the case of the H-Beta

zeolite. At the beginning, the o-DCB decreases and does not stabilise until 5 hours have passed. Thereafter it continues to decrease but very slowly until it stabilises after 24 hours. At this time, the o-DCB conversion is 40%, 55%, 27% and 63% for the alumina, titania, H-ZSM5 and H-Beta supported catalysts, respectively. The o-DCB light-off curve at 300 ºC exhibits conversions of 77%, 65%, 58% and 80%, respectively. Thus, as it is seen, the alumina and the H-ZSM5 are the ones most negatively affected by time-deactivation.

The results exposed evidenced that the deactivation of catalyst affects both reactions, although specially o-DCB oxidation. o-DCB oxidation reaction undergo the most significant deactivation. According to literature, no evidences of deactivation have been reported in SCR in the absence of o-DCB (Yao et al., 2017); thus, deactivation of the catalysts is probably strongly related to o-DCB oxidation. It is well known that oxidation of chlorinated compounds promotes deactivation effects in different types of catalysts at low temperature. Kan et al. associated the low-temperature deactivation of MnO_X-CeO_2 catalysts in the oxidation of chlorobenzene to the adsorption of Cl on the active sites (Kan et al., 2017). If this was the case, it makes sense that the catalyst supported on H-Beta presents the best stability. 20% MnO_X-CeO_2/H-Beta is the catalyst which presents the highest surface area. What is more, this high surface area is composed of mesopores. Due to these two reasons, it is the catalyst in which it is the most difficult to block the active sites with chlorine and carbon adsorption (Martín-Martín et al., 2020).

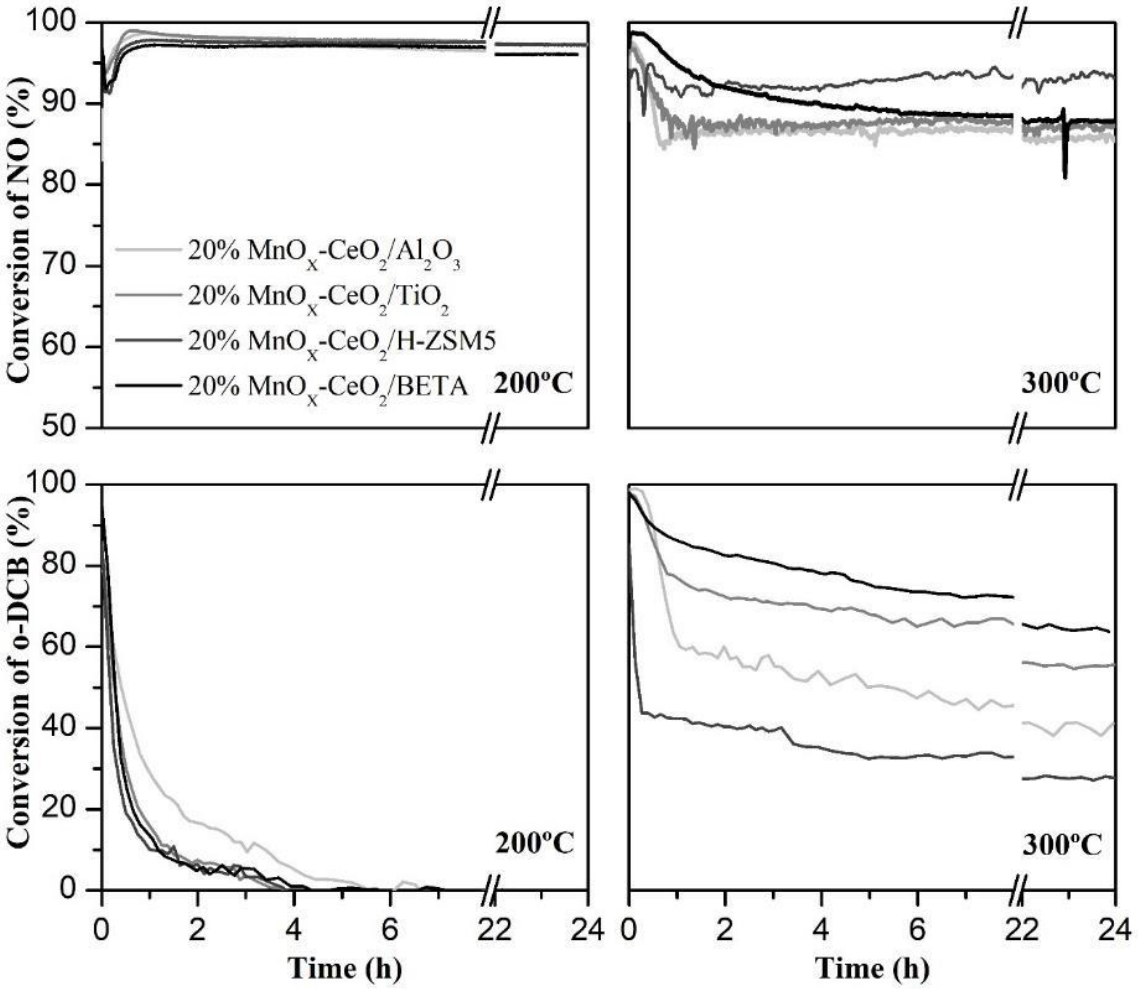

Figure 19: Stability tests of 20% MnO_X-CeO_2 load supported catalysts.

Taking all the results of catalytic activity into account, it has been concluded that the best support is the H-Beta. Thus, the best catalyst is 20% MnO_X-CeO_2/H-Beta. This decision has been taken because it is the catalyst which shows the widest temperature range of total conversion in both SCR and oxidation reaction. In fact, from 333 to 380 ºC total conversion is reached in the two abatement reactions, which in the rest of the supports does not occur. Besides, it is the one which produces the least by-products in the SCR reaction and it also presents good results in the stability tests. The only drawback it presents is the formation of the oxidation reaction by-products, which are superior compared to the rest of the supports. Nevertheless, the positive aspects outweigh this drawback. The good results of the 20% MnO_X-CeO_2/H-Beta catalyst are linked to a high extent to its high surface area (which is the highest one), to its pore size distribution composed mainly of mesopores and to its good acid and redox properties, promoted by a high interaction and dispersion of the active phase.

For this reason, the formation of by-products in the stability-test has been only analysed for the 20% MnO_X-CeO_2/H-Beta. It should be noted that this has also been done for the other catalysts although results have not been shown because they follow a similar trend. Results are presented in Figure 20. In this figure it is represented the conversion results obtained for the SCR and oxidation reaction to facilitate the understanding.

Regarding the by-products of the SCR reaction no NO_2 formation is observed after 30-45 minutes. This is because as previously analysed, NO_2 forms above 300 ºC. On the other hand, N_2O formation depends on the temperature of the stability test. When the experiment is performed at 200 ºC, a remarkable drop of N_2O concentration is observed with time, starting at 75 ppm, and ending up, after 22 hours, at 20 ppm. This deactivation of N_2O-producing side reactions could be related to deactivating species inhibiting o-DCB conversion. Contrastingly, at 300 ºC, N_2O formation increases with time, reaching a value of 75 ppm.

Regarding the oxidation reaction, after four hours the loss o-DCB oxidation conversion is observed at 200 ºC, which is in accordance with the decrease of CO and CO_2, indicating that the oxidation of o-DCB is not taking place. Nevertheless, at 300 ºC the conversion of o-DCB stabilises at 64%. This indicates and confirms that this range of temperatures favour the oxidation reaction and suggests that catalysts are deactivated in the oxidation of chlorobenzene at temperatures below 300 °C. The formation of CO_2 decreases with time and the formation of by-products increases. This indicates that at 300 ºC a change in the oxidation reaction mechanism happens over time. The sharp drop in CO_2 and the rise of the by-products coincide in the first hour of the experiment. This suggests that there are some early active centres that deactivate quickly, which could be the ones that gave the reaction in one way (no producing by-products, achieving total oxidation). When these centres have deactivated the reaction occurs by the other mechanism producing more by-products. Hence, the reaction becomes less selective towards total oxidation. Thus, different types of active centres are involved, and the mechanism is different in each of them.

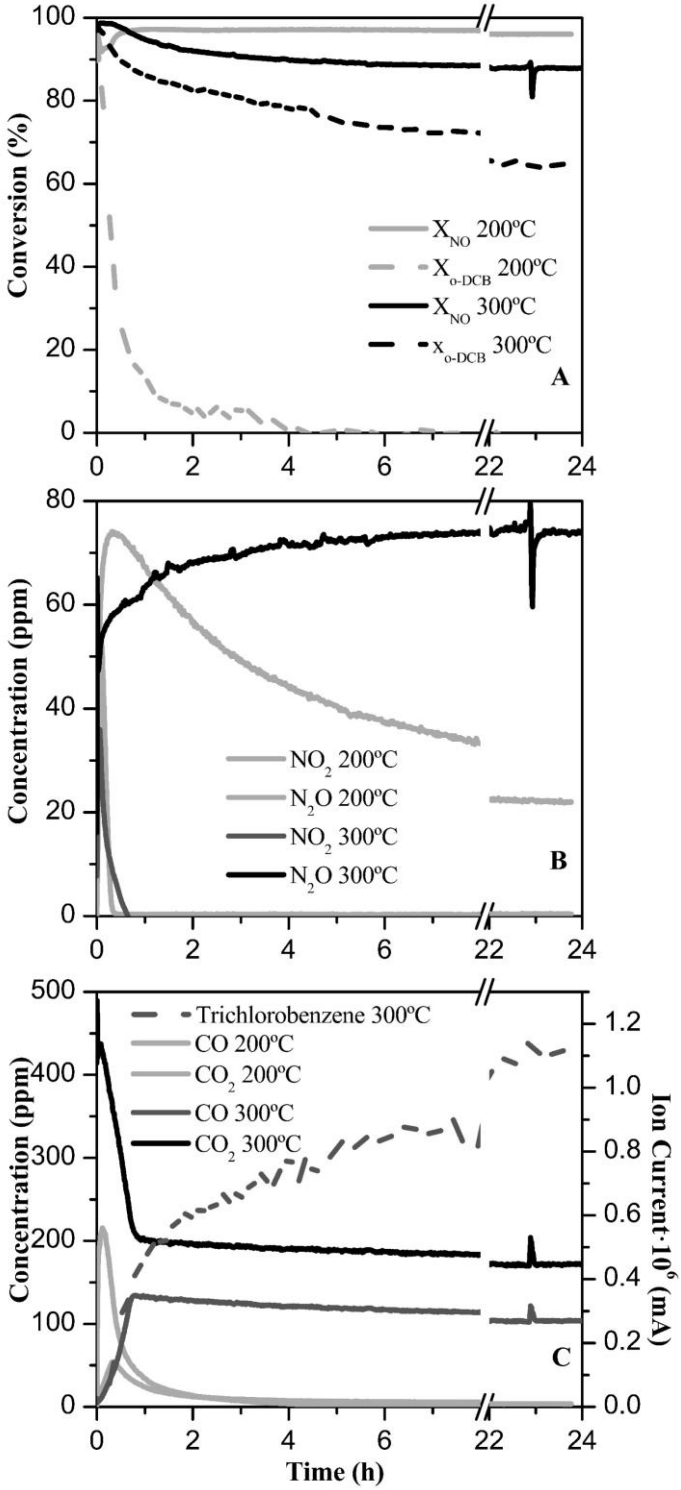

Figure 20: Stability-test for the 20% MnO_X-CeO_2/H-Beta catalyst: A) conversions reached in the simultaneous abatement reactions, B) formation of by-products in the SCR reaction and C) formation of by-products and product of the oxidation reaction.

5. CONCLUSIONS

After having analysed the results obtained and regarding the proposed objectives, the summary of the main conclusions is the following one:

Firstly, MnO_X-CeO_2 active phase deposition has been successfully synthesised by the co-precipitation method on the four supports, alumina, titania, H-ZSM5 and H-Beta. The co-precipitation method has also allowed to obtain a high dispersion of the active phase, as evidenced by SEM and STEM-HAADF techniques. In addition, XRD has also evidenced the good dispersion of the active phase. However, XRD also showed that at high active phase loadings, the active phase can agglomerate in some areas reaching sizes of 8 nm.

The load of active phase has a clear effect on the reaction results, favouring the simultaneous abatement of NO and o-DCB as this load increases. In the SCR reaction, the increase of the active phase allows NO conversions higher than 90% to be achieved at lower temperatures. In the o-DCB oxidation, the increase of active phase shifts the ignition curves to lower temperatures, independently to the support. Hence, the same o-DCB conversions are achieved at lower temperatures when the active phase load increases.

The improvements promoted by the active phase in catalytic activity are associated to the higher oxidative capacity promoted by the active phase due to better mobility of oxygen. This oxygen mobility is promoted by the interaction of the metals that compose the active phase, as well as by the interaction between the active phase and the support, that generate structural defects, favouring the formation of oxygen vacancies. This is evidenced by NH_3-TPD technique, where it is seen how the strong acidity increases with the active phase. The aforementioned interaction also contributes to two fundamental factors, on the one hand, to the improvement of the redox properties, i.e., the lower reduction temperatures with respect to the bare MnO_X-CeO_2, and to the appearance of different Mn species with high oxidation state, both factors have been evidenced by H_2-TPR and are fundamental for the SCR reaction.

The use of different supports also affects the catalytic activity. The alumina support allows to obtain higher NO conversions at lower temperatures. In fact, in the 20% MnO_X-CeO_2/Al_2O_3 catalyst, as well as in the 20% MnO_X-CeO_2/TiO_2 catalyst, the conversions are similar to those of the unsupported active phase. On the other hand, zeolites show higher activity in the SCR at higher temperatures compared to the bare MnO_X-CeO_2, which is more noticeable in the catalysts supported on H-Beta. This fact allows to widen the temperature range where NO conversions above 90% are obtained.

Regarding the o-DCB oxidation, 20% MnO_X-CeO_2/H-Beta is the catalysts which reaches total conversion of o-DCB at the lowest temperature. This fact, together with the results of the SCR reactions, give the H-Beta the chance to have total conversion in both SCR and oxidation reaction from 333 to 380 ºC. It also shows good stability under these conditions. These good results make the support H-Beta improve the catalytic performance compared to bare MnO_X-CeO_2. This improvement is attributed to its high surface area, to its pore size distribution composed mainly of mesopores and to its good acid and redox properties.

The selectivity analysis has shown that the support affects the formation of by-products in both reactions. N_2O and NO_2 are the main by-products of the SCR reaction, mainly generated when the active phase is deposited, thus, the active phase is what generates them. While N_2O is produced over the whole temperature range, NO_2 is only produced at high temperatures. All the supported catalysts produce less N_2O and NO_2 than the bare MnO_X-CeO_2, what means that the

selectivity of the SCR reaction is improved. In the oxidation reaction the main by-product is CO, generated in all the catalysts, independently to the support. In addition, small amounts of chlorinated organic by-products have been detected on catalysts supported on zeolites.

Taking all this into account, the simultaneous abatement of NO and o-DCB is feasible with the use of a support. In fact, comparing to the results achieved without supporting the active phase, similar or in some aspects even better results are obtained. Based on NH_3-SCR and o-DCB oxidation reaction results, 20% MnO_X-CeO_2 is found to be the optimum load of active phase and H-Beta the optimum support.

6. NOMENCLATURE

C_{A0}	Concentration of the reagent at the entrance of the reactor (ppm)
C_A	Concentration of the reagent at the outlet the reactor (ppm)
d	Spacing of the lattice planes (nm)
K	Constant of the Scherrer equation (dimensionless)
L	Thickness of the crystallite (nm)
N	Number of lattice planes (dimensionless)
P/P_0	Relative pressure (dimensionless)
x_A	Conversion of the reagent (%)
ΔV/ΔD	Adsorbed volume regarding the pore diameter ($cm^3/(g \cdot nm)$)
Δ(2Θ)	Width of the X-ray reflection (º)
Θ_0	Bragg's angle (º)
λ	Wavelength (nm)

Acronyms and abbreviations

BET	Brunauer, Emmett and Teller
BJH	Barrett, Joyner and Halenda
EDXS	Energy Dispersive X-Ray Spectroscopy
GC-MS	Gas Chromatograph equipped with a Mass Selective detector
HAADF	High Angle Annular Dark Field
INMA	Institute of Nanoscience and Materials of Aragon
IUPAC	International Union of Pure and Applied Chemistry
MSW	Municipal Solid Waste
MSWI	Municipal Solid Waste Incineration
NO_X	Nitrogen oxides
o-DCB	1,2-dichlorobenzene
PCDDs	Polychlorinated dibenzo-p-dioxins
PCDFs	Polychlorinated dibenzo-p-furans

PCDD/Fs	Polychlorinated dibenzo-p-dioxins and polychlorinated dibenzo-p-furans
PLC	Programmable Logic Controller
SCR	Selective Catalytic Reduction
SEM	Scanning Electron Microscopy
SNCR	Selective Non Catalytic Reduction
STEM	Scanning Transmission Electron Microscopy
TCD	Thermal Conductivity Detector
TEM	Transmission Electron Microscopy
TEQ	Toxicity Equivalent Factor
TPD	Temperature Programmed Desorption
TPR	Temperature Programmed Reduction
TQSA	Chemical Technologies for Environmental Sustainability
VOC	Volatile Organic Compounds
WDXFR	X-Ray Fluorescence Spectrometry by the Dispersion of Wavelengths
XRD	X-Ray Diffraction
XRF	X-Ray Fluorescence Spectrometry

7. REFERENCES

Alothman, Z.A., 2012. A review: Fundamental aspects of silicate mesoporous materials. *Materials,* **5**(12), pp. 2874-2902.

Anderson, J., Boudart, M.,1984. Catalysis, Science and Technology. Volume 5. Springer-Verlag, Berlin, Heidelberg.

Aracil, C., Haro, P., Fuentes-cano, D. and Gómez-Barea, A., 2018. Implementation of waste-to-energy options in landfill-dominated countries: Economic evaluation and GHG impact. *Waste Management,* **76**, pp. 443-456.

Younes, B.N., Ortigosa, J.M., Marie, O., Blasco, T. and Mhamdi, M., 2021. Effect of zeolite structure on the selective catalytic reduction of NO with ammonia over Mn-Fe supported on ZSM-5, BEA, MOR and FER. *Research on Chemical Intermediates,* **47**(5), pp. 2003-2028.

Boningari, T., Ettireddy, P.R., Somogyvari, A., Liu, Y., Vorontsov, A., Mcdonald, C.A. and Smirniotis, P.G., 2015. Influence of elevated surface texture hydrated titania on Ce-doped Mn/TiO2 catalysts for the low-temperature SCR of NOx under oxygen-rich conditions. *Journal of Catalysis,* **325**, pp. 145-155.

Bonte, J.L., Fritsky, K.J., Plinke, M.A. and Wilken, M., 2002. Catalytic destruction of PCDD/F in a fabric filter: experience at a municipal waste incinerator in Belgium. *Waste Management,* **22**(4), pp. 421-426.

Botas, J.A., Serrano, D.P., García, A., De vicente, J. and Ramos, R., 2012. Catalytic conversion of rapeseed oil into raw chemicals and fuels over Ni- and Mo-modified nanocrystalline ZSM-5 zeolite. *Catalysis Today,* **195**(1), pp. 59-70.

Bratan, V., Munteanu, C., Hornoiu, C., Vasile, A., Papa, F., State, R., Preda, S., Culita, D. and Ionescu, N.I., 2017. CO oxidation over Pd supported catalysts —In situ study of the electric and catalytic properties. *Applied Catalysis B: Environmental,* **207**, pp. 166-173.

Degraeuwe, B., Thunis, P., Clappier, A., Weiss, M., Lefebvre, W., Janssen, S. and Vranckx, S., 2016. Impact of passenger car NOx emissions and NO2 fractions on urban NO2 pollution – Scenario analysis for the city of Antwerp, Belgium. *Atmospheric environment (1994),* **126**, pp. 218-224.

Directive 2008/98/EC of the European Parliament and of the Council of 19 November 2008 on waste and repealing certain Directives. 2008. Official Journal of the European Union. L 312/3.

Directive 2010/75/EU of the European Parliament and of the Council of 24 November 2010 on industrial emissions (integrated pollution prevention and control). 2010. Official Journal of the European Union. L 334/17.

Directive (EU) 2018/851 of The European Parliament and of The Council of 30 May 2018 , amending Directive 2008/98/EC on waste. Official Journal of the European Union. L 150/109.

El Mragui, A., Zegaoui, O., Daou, I. and Esteves Da Silva, J. C. G., 2021. Preparation, characterization, and photocatalytic activity under UV and visible light of Co, Mn, and Ni

mono-doped and (P,Mo) and (P,W) co-doped TiO2 nanoparticles: a comparative study. *Environmental Science and Pollution Research*, **28**(20), pp. 25130-25145.

Eurostat. European Statistical Office. (Available on: https://ec.europa.eu/eurostat) [Access: 15/06/2021].

Fermanelli, C.S., Pierella, L.B. and Saux, C., 2021. Comparative study of zeolites matrices in bio-wastes pyrolytic valorization. *Process Safety and Environmental Protection*, **147**, pp. 808-817.

Finocchio, E., Busca, G. and Notaro, M., 2006. A review of catalytic processes for the destruction of PCDD and PCDF from waste gases. *Applied Catalysis B: Environmental*, **62**(1), pp. 12-20.

Gallastegi-Villa, M., 2016. VOx/WOx/TiO2 and alternative catalysts for the simultaneous abatement of NOx and PCDD/Fs from MSW treatment plants. PhD Dissertation. UPV/EHU, Leioa.

Gallastegi-Villa, M., Aranzabal, A., Boukha, Z., González-Marcos, J.A., González-Velasco, J.R., Martínez-Huerta, M.V. and Bañares, M.A., 2015. Role of surface vanadium oxide coverage support on titania for the simultaneous removal of o-dichlorobenzene and NOx from waste incinerator flue gas. *Catalysis Today*, **254**, pp. 2-11.

Gallastegi-Villa, M., Aranzabal, A., González-Marcos, M.P., Markaide-Aiastui, B.A., González-Marcos, J.A. and González-Velasco, J.R., 2020. Effect of vanadia loading on acidic and redox properties of VOx/TiO2 for the simultaneous abatement of PCDD/Fs and NOx. *Journal of Industrial and Engineering Chemistry*, **81**, pp. 440-450.

Goemans, M., Clarysse, P., Joannes, J., De Clercq, P., Lenaerts, S., Matthys, K and Boels, K., 2004. Catalytic NOx reduction with simultaneous dioxin and furan oxidation. *Chemosphere*, pp. 1357-1365.

Gonçalves, A.A.S., Ciesielczyk, F., Samojeden, B. and Jaroniec, M., 2021. Toward development of single-atom ceramic catalysts for selective catalytic reduction of NO with NH3. *Journal of hazardous materials*, **401**, pp. 123413.

Groen, J.C., Peffer, L.A.A. and Pérez-Ramírez, J., 2003. Pore size determination in modified micro- and mesoporous materials. Pitfalls and limitations in gas adsorption data analysis. *Microporous and Mesoporous Materials*, **60**(1), pp. 1-17.

Gu, T., Yin, C., Ma, W. and Chen, G., 2019. Municipal solid waste incineration in a packed bed: A comprehensive modeling study with experimental validation. *Applied Energy*, **247**, pp. 127-139.

Hwang, I., Minoya, H., Matsuto, T., Matsuo, T., Matsumoto, A. and SAMESHIMA, R., 2009. Removal of ammonium chloride generated by ammonia slip from the SNCR process in municipal solid waste incinerators. *Chemosphere*, **74**(10), pp. 1379-1384.

Ibarbia, A., 2017. MnOX-CeO2 as an alternative catalyst for the simultaneous abatement of NOx and PCDD/Fs from MSW treatment plants. Feasibility and reaction pathways study. Bachelor Final Project, UPV/EHU. Leioa.

Jiménez, J.A., Padilla, I., Lõpez-DelGado, A., Fillali, L. and Lõpez-Andrés, S., 2015. Characterization of the aluminas formed during the thermal decomposition of boehmite by the rietveld refinement method. *International Journal of Applied Ceramic Technology,* **12**(S2), pp. E178-E186.

Kan, J., Deng, L., Li, B., Huang, Q., Zhu, S., Shen, S. and Chen, Y., 2017. Performance of co-doped Mn-Ce catalysts supported on cordierite for low concentration chlorobenzene oxidation. *Applied Catalysis A: General,* **530**, pp. 21-29.

Kang, M., YeoN, T.H., Park, E.D., Yie, J.E. and Kim, J.M., 2006. Novel MnO x catalysts for NO reduction at low temperature with ammonia. *Catalysis Letters,* **106**(1-2), pp. 77-80.

Li, J., Shi, Y., Fu, X., Shu, Y., Huang, J., Zhu, J., Tian, G. and Hu, J., 2021a. Effects of Ni substitution on active oxygen species and electronic interactions over La0.8Ce0.2MnO3/mesoporous ZSM-5 for oxidizing C6H14. *Molecular Catalysis,* **499**, pp. 111309.

Li, M., Zhou, Y., Wang, G., Zhu, G., Zhou, X., Gong, H., Sun, J., Wang, L. and Jinsong Liu, 2021b. Evaluation of atmospheric sources of PCDD/Fs, PCBs and PBDEs around an MSWI plant using active and passive air samplers. *Chemosphere,* **274**, pp. 129685.

Lin, X., Ma, Y., CheN, Z., Li, X., Lu, S. and Yan, J., 2020. Effect of different air pollution control devices on the gas/solid-phase distribution of PCDD/F in a full-scale municipal solid waste incinerator. *Environmental Pollution,* **265**.

Liu, X., Wang, J., Wang, X. and Zhu, T., 2015. Simultaneous removal of PCDD/Fs and NOx from the flue gas of a municipal solid waste incinerator with a pilot plant. *Chemosphere,* **133**, pp. 90-96.

Liu, Y., Hou, Y., Han, X., Wang, J., Guo, Y., Xiang, N., Bai, Y. and Huang, Z., 2020. Effect of Ordered Mesoporous Alumina Support on the Structural and Catalytic Properties of Mn−Ni/OMA Catalyst for NH3−SCR Performance at Low-temperature. *ChemCatChem,* **12**(3), pp. 953-962.

Liu, Z., Yi, Y., Zhang, S., Zhu, T., Zhu, J. and Wang, J., 2013. Selective catalytic reduction of NOx with NH3 over Mn-Ce mixed oxide catalyst at low temperatures. *Catalysis Today,* **216**, pp. 76-81.

López-Fonseca, R., 2001. Zeolitas protónicas (h-y, h-zsm-5 y h-mor) para la destrucción catalítica de compuestos orgánicos volátiles clorados. PhD Dissertation. UPV/EHU, Leioa.

Ma, Z., Zaera, F., 2014. Surface and Nanomolecular Catalysis. Characterization of Heterogeneous Catalysts. Taylor & Francis (CRC Press), pp.1-37.

Martín-Martín, J.A., Gallastegi-Villa, M., González-Marcos, M.P., Aranzabal, A. and González-Velasco, J.R., 2021a. Bimodal effect of water on V2O5/TiO2 catalysts with different

vanadium species in the simultaneous NO reduction and 1,2-dichlorobenzene oxidation. *Chemical Engineering Journal*, **417**, pp. 129013.

Martín-Martín, J.A., Gallastegi-Villa, M., González-Marcos, M.P., AranzabaL, A. and González-Velasco, J.R., 2021b. Effect of Mn/Ce ratio in MnOX-CeO2 catalysts for the simultaneous abatement of NOX and o-DCB. Manuscript in preparation.

Martín-Martín, J.A., Sánchez-Robles, J., González-Marcos, M.P., Aranzabal, A. and González-Velasco, J.R., 2020. Effect of preparation procedure and composition of catalysts based on Mn and Ce oxides in the simultaneous removal of NOX and o-DCB. *Molecular Catalysis,* **495**, pp. 111152.

Ministry for Ecological Transition and the Demographic challenge. 2018. Memoria anual de generación y gestión de residuos, residuos de competencia municipal.

Neuwahl, F., Cusano, G., Gomez-Benavides, J., Holbrook, S., Roudier, S., 2019. Best Available Techniques (BAT) Reference Document for Waste Incineration. *European Commission.* 10.2760/761437

Qian, L., Wang, Y., Liu, M., Hu, Y., Chun, T., Meng, Q., Long, H. and Wang, Y., 2021. Performance evaluation of urea injection on the emission reduction of dioxins and furans in a commercial municipal solid waste incinerator. *Process Safety and Environmental Protection,* **146**, pp. 577-585.

Quindimil-Rengel, A. 2015. Influencia del soporte y carga metálica en catalizadores Ni/Zeolita sobre la actividad de hidrogenación de CO_2 para producción de metano. Master Degree Final Project, UPV/EHU, Leioa.

Santos, V.P., Pereira, M.F.R., Orfao, J.J.M. and Figueiredo J.L., 2010. The role of lattice oxygen on the activity of manganese oxides towards the oxidation of volatile organic compounds. *Applied Catalysis B: Environmental,* pp. 353-363.

Schecter, A., Gasiewich, T.A., 2003. Dioxins and Health, 2nd ed. John Wiley & Sons, Inc., Hoboken, New Jersey.

Shen, Q., Zhang, L., Sun, N., Wang, H., Zhong, L., He, C., Wei, W. and Sun, Y., 2017. Hollow MnOx-CeO2 mixed oxides as highly efficient catalysts in NO oxidation. *Chemical Engineering Journal,* **322**, pp. 46-55.

Sun, J., Chen, H., Wu, H., Zhou, C. and Yang, H., 2019. Enhanced low-temperature Selective Catalytic Reduction (SCR) of NOx by CuO-CeO2-MnOx/Γ-Al2O3 mixed oxide catalysts. *Canadian Journal of Chemical Engineering*, **97**(9), pp. 2498-2504.

Tae, S.P., Soon, K.J., Sung, H.H and Sung, C.H., 2001. Selective catalytic reduction of nitrogen oxides with NH 3 over natural manganese ore at low temperature. *Industrial and Engineering Chemistry Research*, **40**(21), pp. 4491-4495.

Tang, X., Wang, C., Gao, F., Han, W., Yi, H., Zhao, S., Zhou, Y. and Liu, Y., 2021. Mn-Fe-Ce multiple oxides with Al2O3 coating supported onto honeycomb cordierite monoliths for NO

catalytic oxidation. *Colloids and Surfaces A: Physicochemical and Engineering Aspects,* **611**, pp. 125790.

Van Caneghem, J., Van Acker, K., De Greef, J., Wauters, G. and Vandecasteele, C., 2019. Waste-to-energy is compatible and complementary with recycling in the circular economy. *Clean Technologies and Environmental Policy*.

Wang, C., Lee, W.J., Tsai, P.J., Lee, W.S. and Chang-Chien, P.G, 2003. Emissions of polychlorinated dibenzo-p-dioxins and dibenzofurans from stack flue gases of sinter plants. *Chemosphere*, pp. 1123-1129.

Wang, C., Yu, F., Zhu, M., Tang, C., Zhang, K., Zhao, D., Dong, L. and dai, B., 2019. Highly selective catalytic reduction of NOx by MnOx–CeO2–Al2O3 catalysts prepared by self-propagating high-temperature synthesis. *Journal of Environmental Sciences,* **75**, pp. 124-135.

Wang, X., Kang, Q. and Li, D., 2008. Low-temperature catalytic combustion of chlorobenzene over MnOx–CeO2 mixed oxide catalysts. *Catalysis Communications,* **9**(13), pp. 2158-2162.

Wei, L., Chen, H., Wei, Y., Jia, J. and Zhang, R., 2021. Ce-promoted Mn/ZSM-5 catalysts for highly efficient decomposition of ozone. *Journal of Environmental Sciences*, **103**, pp. 219-228.

Xu, W., Zhang, G., Chen, H., Zhang, G., Han, Y., Chang, Y. and Gong, P., 2018. Mn/beta and Mn/ZSM-5 for the low-temperature selective catalytic reduction of NO with ammonia: Effect of manganese precursors. *Chinese Journal of Catalysis,* **39**(1), pp. 118-127.

Xu, W., Wang, Y., Li, S., Cheng, Y., Yan, F., Hu, L., Liao, M., Peng, J. and Guo, Z., 2021. ZSM-5(8T)@γ-Al2O3 supported AlCl3 core-shell catalyst: Mechanism research on disproportionation reaction of methylchlorosilanes. *Inorganica Chimica Acta,* **516**, pp. 120148.

Yao, X., Ma, K., Zou, W., He, S., An, J., Yang, F. and Dong, L., 2017. Influence of preparation methods on the physicochemical properties and catalytic performance of MnOx-CeO2 catalysts for NH3-SCR at low temperature. *Chinese Journal of Catalysis,* **38**(1), pp. 146-159.

Zabalgarbi. Official webpage of the Zabalgarbi MSWI plant. (Available on: http://www.zabalgarbi.com/es/) [Access: 15/06/2021].

Zeng, X., Wang, Z., Ding, J., Wang, L., Jiang, Y., Stampfl, C., Hunger, M. and Huang, J., 2019. Catalytic arene alkylation over H-Beta zeolite: Influence of zeolite shape selectivity and reactant nucleophilicity. *Journal of Catalysis,* **380**, pp. 9-20.

Zhan, M., Chen, T., Lin, X., Fu, J., Li, X., Yan, J. and Buekens, A., 2016. Suppression of dioxins after the post-combustion zone of MSWIs. *Waste Management,* **54**, pp. 153-161.

Zhang, G., Huang, X. and Tang, Z., 2019a. New insight into the synergistic promotion effect of phosphorus and molybdenum on the ceria-titanium catalysts for superior SCR performance. *Molecular Catalysis,* **478**, pp. 110562.

Zhang, Z., Wu, J., Li, B., Xu, H. and Liu, D., 2019b. Removal of elemental mercury from simulated flue gas by ZSM-5 modified with Mn-Fe mixed oxides. *Chemical Engineering Journal,* **375**, pp. 121946.

Zhang, M., Yin, D., Guo, J., Wu, H., Gong, M. and Feng, X., 2021. Ternary catalyst Mn-Fe-Ce/Al2O3 for the ozonation of phenol pollutant: performance and mechanism. *Environmental Science and Pollution Research*.